An Implantable Radiation Detector for Cancer Radiotherapy

Kyoungtae Lee
Michel Maharbiz, Ed.
Mekhail Anwar, Ed.
Ali Niknejad, Ed.
Eric Norman, Ed.

Electrical Engineering and Computer Sciences
University of California, Berkeley

Technical Report No. UCB/EECS-2023-27
http://www2.eecs.berkeley.edu/Pubs/TechRpts/2023/EECS-2023-27.html

May 1, 2023

An Implantable Radiation Detector for Cancer Radiotherapy

by

Kyoungtae Lee

A dissertation submitted in partial satisfaction of the

requirements for the degree of

Doctor of Philosophy

in

Engineering - Electrical Engineering and Computer Science

in the

Graduate Division

of the

University of California, Berkeley

Committee in charge:

Professor Michel M. Maharbiz, Chair
Associate Professor Mekhail Anwar, Co-chair
Professor Ali Niknejad
Professor Eric B. Norman

Summer 2021

An Implantable Radiation Detector for Cancer Radiotherapy

Abstract

An Implantable Radiation Detector for Cancer Radiotherapy

by

Kyoungtae Lee

Doctor of Philosophy in Engineering - Electrical Engineering and Computer Science

University of California, Berkeley

Professor Michel M. Maharbiz, Chair

Associate Professor Mekhail Anwar, Co-chair

This dissertation presents a millimeter-scale CMOS 64×64 single charged particle radiation detector system for cancer radiotherapy; this work is applicable to therapies including external beam radiotherapy (EBRT), targeted radionuclide therapy (TRT), and brachytherapy. We demonstrate 1×1 μm^2 diode pixels capable of measuring energy deposition into a depletion region by single charged particles. These pixels can be arrayed to provide large detection areas; we demonstrate a 512×512 μm^2 array. Instead of sensing the voltage drop caused by radiation, the system measures pulse width, i.e., the time it takes for the voltage to return to its baseline. This obviates the need for power-hungry and large analog-to-digital converters. A prototype ASIC is fabricated in TSMC 65 nm LP CMOS process and consumes the average static power of 0.535 mW under 1.2 V power supply. The functionality of the whole system is successfully verified in a clinical 67.5 MeV proton beam setting, as well as MeV range electrons and X-ray beam produced by linear accelerator.

To my friends and family.

Contents

List of Figures

List of Tables

Acknowledgments

Finally, my journey as a Ph.D student ends. All these works couldn't have been done without a lot of people's help. I would like to take this opportunity to thank everyone.

During my Ph.D, I have been co-advised by Prof. Michel M. Maharbiz and Prof. Mekhail Anwar, and I truly think I am so lucky to have them as my advisors. They both are very patient listening to me. Personally, they are my role models as advisors and mentors.

I believe the most important ability as an engineer is the intuition. Michel's intuition really surprised me many times. When I was struggling to measure proton beam and I failed multiple times, he said the satellite uses polyimide material for insulation and suggested me to look into it because there are a lot of researches about radiation effects on polyimide. When I heard that, I thought that couldn't be the reason. But in the next experiment when I used a collimator to protect the polyimide, the results look surprisingly good. And I was like "how does he even know what the problem of designing a satellite is?" I also appreciate Michel caring my mentality and emotions. Especially during COVID-19, he always tries to check whether I am well.

My first impression about Mekhail is that he is professional and intellectual. I firstly met him in SWARM kitchen, and he explained how important it is to measure radiation in a small scale. Right after that, I was like, "okay I'm in". I wanna give him a credit coming up with this idea. I learned a lot from him how to lead a big interdisciplinary project that uses circuit design, nuclear physics, and radiobiology. Instead of ordering me around, he tries to convince me first if there is something that he wants me to.

Prof. Eric B. Norman helped me out as my qualification exam committee member and continues to be my dissertation committee member. He has been advising me since beginning of my third year when I was looking for a radiation source. Since then, I have met him about at least once every month, and he gave me a lot of valuable advises on nuclear physics. I really love and admire his curiosity. I remember when he put a balloon in liquid nitrogen and I laughed like a child. I also remember he explained about how he detected neutrinos using a giant water tank buried in the ground, and I was astonished by the work that aimed to better understand our world. I learned how incredible the nature is from him.

Prof. Ali Niknejad was one of my qualification exam committee members and he is my dissertation committee member. I thank for many valuable advises during the qualification exam.

I'm pretty sure all Berkeley EECS graduate students thank Shirley Salanio. Not only she helped me about all the paper works and logistics, but she truely takes a good care of graduate students.

Jessica Scholey, Dr. Inder K. Daftari, and Dr. Kavita K. Michra all helped me a lot for proton project. I really appreciate all of them for welcoming me, teaching me, and letting me use the beam. Dr. Bruce A. Faddegon gave me a lot of insights on clinical physics. Discussing with him was always fun.

I'd like to thank Dongjin Seo and Konlin Shen who trained me machines in the lab and helped a lot on settling in. To the rest of the Maharbiz group who I have had the privilege of

working with: Travis Massey, Oliver Chen, Alyssa Zhou, Soner Sonmezoglu, Arda Ozilgen, David Piech, Mauricio Bustamante, Jordan Edmunds, Wentian Mi, Stefanie Garcia, Tom Zajdel, Monica Lin, Amy Liao, and Bochao Lu. Thank you for welcoming and gatherings that made coming into lab fun.

Also, to the Anwar group members: Hossein Najafi, Rohzan Rabbani, Efthymios Papageorgiou, Christos Adamopoulos, Ali Ameri, Averal Kandala, and Micah Roschelle. Thank you all for great conversations and discussions.

Finally, I would like to thank my family, especially my parents, Jaesoon Yoo and Sangki Lee who sacrificed more than I did for my family so that I become who I am. My sister's lovely family, Hyemin Lee, Jaeyong Song, Yeonjoo Song, and Yeone Song, is also a great source for supporting me. Thank you all for always being there, trusting me, and being my safe place.

Chapter 1

Introduction

1.1 Cancer Radiotherapy

Cancer is a group of diseases with abnormally fast and uncontrolled proliferation of cells that can potentially spread to other parts of the body. According to the most recent report from the American Cancer Society, it is estimated that over 1.8 million people will be diagnosed with cancer in the U.S. in 2021. Approximately 600,000 people will die from cancer in 2021 [3]. Cancer treatment includes removal by surgery, radiotherapy, immunotherapy, and chemotherapy. The combination of methods is chosen carefully depending on the site, stage, type, patient characteristics, and size of the tumor.

For most type of cancers, more than half of the treatment incorporates ionizing radiation [4], where the fundamental goal is to deposit sufficient energy (dose) to destroy the tumor cells and stop their proliferation. A key challenge in radiotherapy is to target only the tumor while imparting minimal damage to surrounding normal tissues. Depending on how radiation is used, there are several types of radiotherapy. The following subsections explain widely used radiotherapy methods that are relevant to this work.

External Beam Radiotherapy (EBRT)

To deposit energy in the tumor, radiation can be applied externally using linear accelerators. Deep penetrating X-ray photons, protons, electrons, or even heavier elements such as carbon ions are accelerated to energies ranging from few MeVs to tens of MeVs. Among various types of radiation, X-ray has been most widely used in EBRT. This well-established method encounters several difficulties: 1) X-rays pass through the whole body, leaving unwanted dose in healthy tissues. This can be critical in pediatric cancer, for example, where secondary malignancy results from peripheral dose to sensitive healthy organs; 2) Because the dose from X-rays is highest near the surface, dropping a few percent per centimeter with depth, and the overall X-ray intensity needs to be large to deliver sufficient dose to the tumor.

Due to these issues, *charged particle radiotherapy* has advantages over X-rays. Unlike photons, charged particles deposit the highest dose in a specific location at the end of their

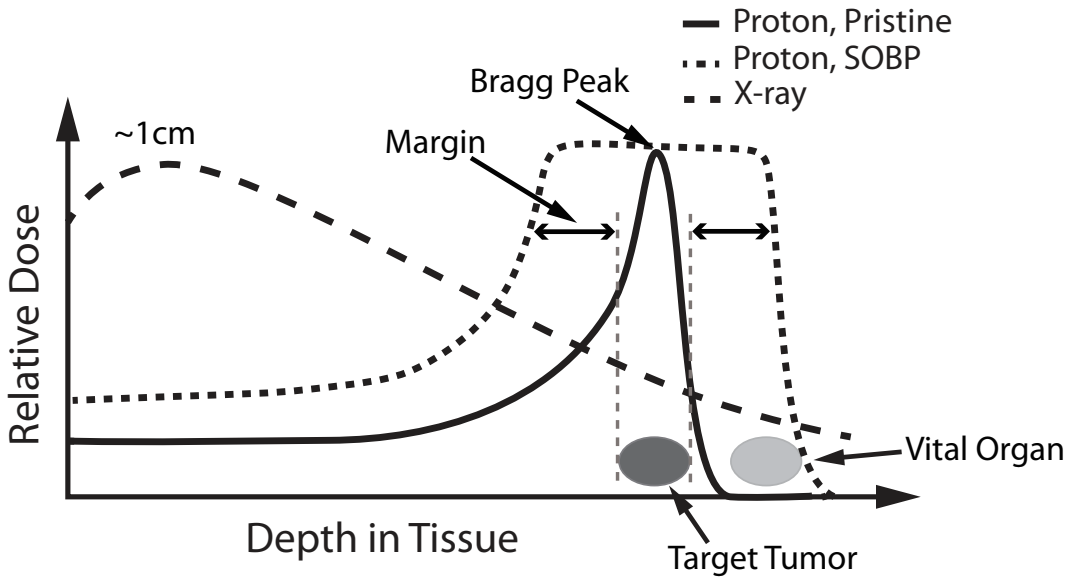

Figure 1.1: Depth-dose curve for X-ray, proton (pristine), and proton (SOBP).

range (the Bragg peak), theoretically allowing dose to be delivered with higher precision and with less peripheral dose than with X-rays (See Fig. 1.1).

Despite the advantages of charged particle therapy, a current limitation is knowing the exact location of the Bragg peak (range uncertainty) which is caused by a number of factors. First, patient movement such as respiratory motion shifts the Bragg peak. Second, charged particle interactions occurring within the body depend heavily on tissue atomic properties, which are difficult to determine accurately [5]. Lastly, day-to-day anatomical variations may make predictions inaccurate. It is difficult to reduce those uncertainties based on a CT image because it is primarily based on the electron density.

The current clinical practice is to mitigate the range uncertainty by using a patient-specific maps of estimated particle stopping power derived from CT image to predict the location of the Bragg peak [6]. However, due to uncertainties in the patient CT image and inaccurate conversion from the CT image to the stopping power, the typical range uncertainty is about 2.5 % of the total range. Given this, it is common in clinics to widen the Bragg peak to cover the full target volume, and then add treatment margins to ensure the target is covered with prescription dose, resulting in increased dose to normal tissue. An example of a spread-out Bragg peak (SOBP) and the additional margins added to account for this range uncertainty is illustrated in Fig. 1.1.

Heavier charged particles (i.e. carbon ion) have narrower and sharper Bragg peaks with better peak to entry dose ratio than protons, theoretically allowing for more accurate targeting the tumors. However, such hadron therapies suffer from worse range uncertainties.

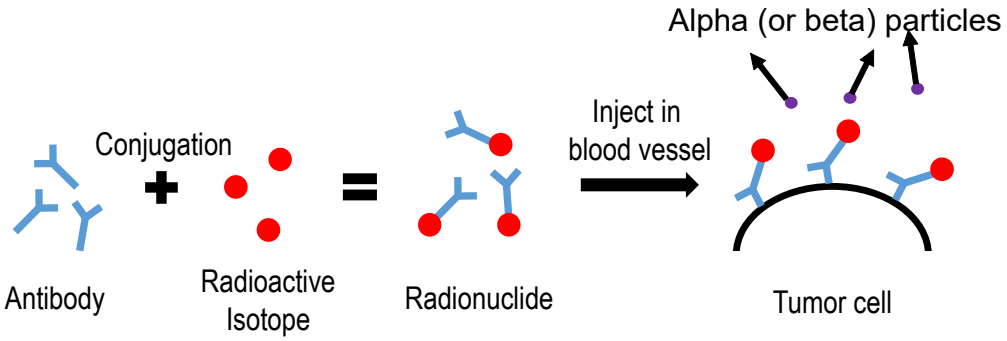

Figure 1.2: Illustration of TRT.

Targeted Radionuclide Therapy (TRT)

In contrast to EBRT, radionuclides conjugated with tumor-specific antibodies are injected intravenously in the body. The antibodies attach to the membranes of cancer cells, and the radidionuclides emit radiation that destroys surrounding cells (See Fig. 1.2). Actinium-225 (Act225, 5.8 MeV alpha decay, and 10 days of half life), thorium-227 (Th227, 6 MeV alpha decay, and 18.7 days of half life), lutetium-177 (Lu177, 497 keV beta decay, and 6.6 days of half life), and yttrium-90 (Y90, 2.28 MeV beta decay, and 2.7 days of half life) are commonly used radionuclides. The choice of radionuclide depends on tumor characteristics. For instance, because alpha particles deposit enormous energy at small distances (< 100 μm), they are used in cases where massive energy deposition in a small concentrated area is needed.

The key challenge in TRT is choosing the right dosing strategy and amount of injection for the patients. Patient specific metabolisms such as the amount and density of antibody receptors, body weight, and biodistributions (i.e. blood volume and flow rate) make "a one-size-fits-all" strategy inadequate in most cases.

The most common method of monitoring the treatment is to use single-photon emission computerized tomography (SPECT) imaging, where nuclear gamma rays resulting from radiation decays are counted externally to estimate tumor uptakes. However, long acquisition time ($\sim$30 minutes) and poor resolution ($\sim$5 mm) preclude monitoring the process over several days, which is necessary to see the full biodistribution of antibodies in the body. For example, in order to determine the total dose delivered to the targets and healthy organs from the treatment, we need following information: 1) the time duration that the dose remains at each site of interest, 2) the rise and decay slopes of the dose, and 3) the maximum dose delivered to the sites.

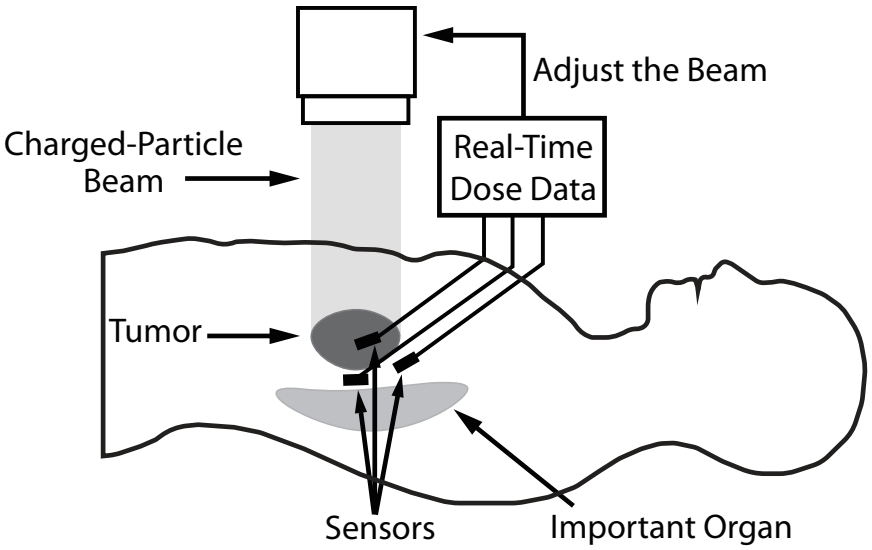

Figure 1.3: Illustration of EBRT with *in vivo* dosimeters.

1.2 *In vivo* Dosimetry (IVD) and its Impact on Radiotherapies

Real-time *in vivo* dosimetry (IVD) ameliorates uncertainty by measuring the dose delivered in the body, potentially leading to more effective and safer closed-loop EBRT (Fig. 1.3). Clinically viable IVDs have several important constraints. They must be millimeter scale for implantation through a standard core-biopsy needle; consume very small amounts of power (to minimize battery size or wireless power transfer requirements); have single-particle sensitivity; be capable of real-time measurement of energy deposition; and be suitable for biocompatible chronic implantation (usually 1-8 weeks) with appropriate medical-grade packaging. These requirements drive the need for a CMOS platform capable of compact integration of low-power sensors and readout circuitry.

While existing approaches have made progress towards miniaturized IVD, no previous work has satisfied all requirements [7–12]. Single MOSFET dosimeters have been the most widely used, as they can be easily fabricated in a small size [7, 8]. Integrated damage by radiation in the SiO_2 layer of the MOSFET decreases the threshold voltage linearly. However, the lifetime is finite and these dosimeters lack single particle sensitivity due to the cumulative nature of the radiation induced damages. Plastic scintillator, thermo-luminescent, or radio-luminescent dosimeters detect light intensity when a radio-sensitive material is exposed to radiation [9,12]. However, they measure only cumulative dose, cannot provide real-time data, and require bulky optical equipment to measure light that precludes implantation. Floating gate dosimeters measure the current change when charges are trapped in the floating gate by radiation [10], but they lack single particle sensitivity.

Most importantly, conventional dosimeters measure average dose, and ignore a critical phenomenon: for a given dose, a single high linear-energy-transfer (LET, energy deposition per unit length) particle has a significantly different biological effect on tissue than that of several low LET particles [13, 14]. The key metric to the biological effect is the energy deposition by each particle. Because the biological effect versus energy deposition is non-linear, the cumulative damage does not represent the true biological effect by radiation. For example, the normalized average number of lethal lesions in a HF19 human diploid fibroblasts cell produced by a single 4, 50, and 70 keV/μm LET alpha-particle is approximately 1, 34.4, and 65.6, respectively [13]. The biological effect increases more rapidly than the energy deposition. The biological effect plateaus after 100 keV/μm. Due to this non-linear relationship between the energy deposition and the biological effect, single particle detection will be a key feature for next-generation IVDs, enabling analysis of the true biological effect by radiation.

The proposed work solves these challenges by introducing a 64×64 pixel implantable millimeter scale single charged particle CMOS dosimeter with the form factor and power consumption compatible with *in vivo* implantation. The ability of providing real-time dose information to single particle sensitivity is envisioned to significantly improve the effectiveness and safety of EBRT and TRT. For example, during EBRT, physicists can monitor the dose information in the tumor and proxy organs to adjust the beam settings (i.e. energy, direction, and flux) accordingly, or even stop the beam when it is mistreating due to patient motion.

1.3 Thesis Organization

The primary goal of this work is to demonstrate a unique IVD that monitors true dose information in the body.

Chapter 2 provides a technical background including how charged particles and photons interact and deposit energy when passing through matter. How a diode can achieve the single charged particle detection is also described. Time domain sampling, as opposed to voltage domain sampling, is introduced and its advantages and a statistical model are covered.

Chapter 3 explains the system, including pixel and pixel array design considerations as well as digital design considerations. A differential sensing scheme is discussed. How we handled pixel-to-pixel variation by using in-pixel SRAM is explained.

Chapter 4 gives electrical noise and pixel-to-pixel variation measurement results. The functionality of the prototype device is verified using clinical proton and electron beam, Lu-177 beta-particle radionuclide solution, and X-ray beam.

Chapter 5 concludes the dissertation with future research directions.

Chapter 2

Theory of Operation

This chapter describes how charged particles and photons interact and deposit energy in a matter, and how the deposited energy relates to the biological effect. The expected signal measured by a diode is analyzed. Finally, the acquisition of a pulse width (as opposed to a voltage level measurement) is discussed.

2.1 Charged Particle Interaction with Matter

With the clinically-relevant energy range, charged particles deposit energy when passing through matter by three types of interactions: 1) Coulomb interactions with atomic electrons; 2) Coulomb interactions with atomic nuclei; and 3) nuclear reactions accompanied by creation of secondary particles (proton, neutron, electron, and gamma ray) [5]. The first type is the most dominant type of interaction, where a charged particle ionizes matter, transferring part of its energy to electrons that deposit their energy in proximity to the point of ionization ($\sim 1\,\text{mm}$). The second type alters the particle trajectory and contributes to scattering. The last type is the rarest. In the first type, LET describes the average amount of charged particle energy deposited per unit length, and is well-modeled by the Bethe-Bloch equation.

$$\frac{dE_{dep}}{dx} \propto \rho \frac{Z}{A} \frac{1}{\beta^2} \left[\ln \frac{2m_e c^2 \gamma^2 \beta^2}{I} - \beta^2 - \frac{\delta}{2} - \frac{C}{Z} \right], \tag{2.1}$$

where dE_{dep}/dx is the energy deposition per unit length, ρ is the density of the absorbing material, Z is the atomic number of the absorbing material, A is the atomic weight of the absorbing material, $\beta = v/c$ where v is the velocity of the proton and c is the speed of light, m_e is the electron mass, $\gamma = (1 - \beta^2)^{-1/2}$, I is the average ionization potential of the absorbing material, δ is the density correction term, and C is the shell correction term [5].

Fig. 2.1 shows LET of protons and electrons in water, data from National Institute of Standards and Technology (NIST) PSTAR and ESTAR [15, 16]. The graphs and Eq. 2.1

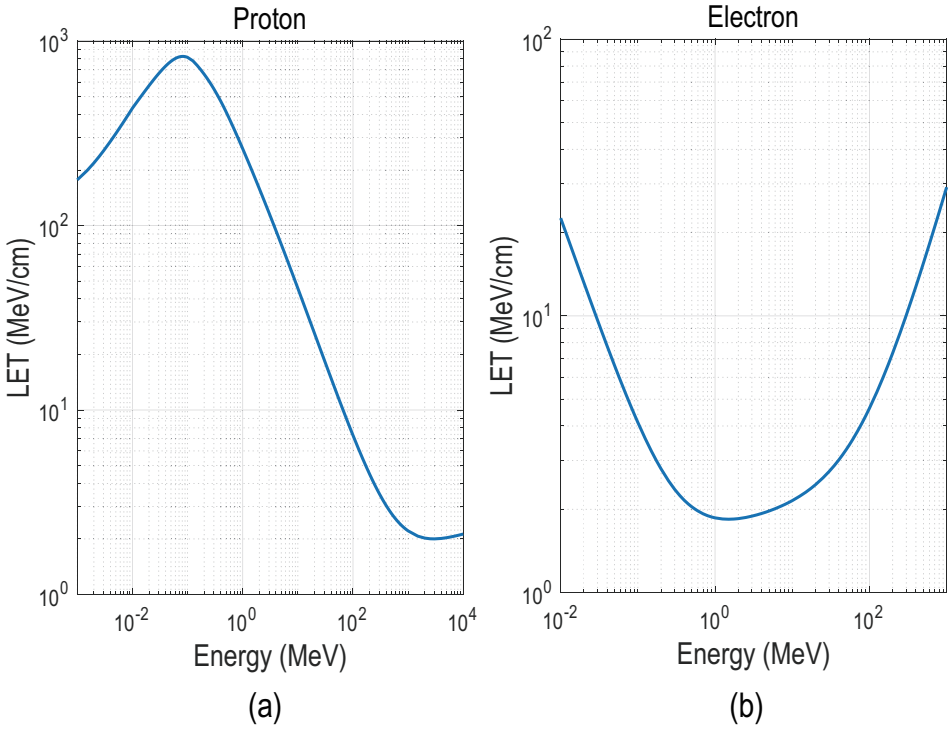

Figure 2.1: LET of protons and electrons in water (Adapted from NIST PSTAR [15] and ESTAR [16]).

show why it is challenging to predict the location of the Bragg peak and particle range, as the LET value heavily depends on the material property and energy of the charged particle.

Dose (Gy = J/kg) is widely used in clinical applications to quantify the radiation effect on tissue:

$$Dose = \sum_{i=1}^{N} \frac{E_{dep,i}}{m} = \frac{\mathbb{E}[E_{dep}] \times N}{m}, \tag{2.2}$$

where N is the number of protons, $E_{dep,i}$ is the energy deposition by each proton in the material, and m is the mass of material where the energy deposition occurred. Dose is the sum of individual energy depositions per unit mass. However, the actual biological effect (e.g., the number of double strand breaks in the DNA or cell mortality rate) for particles with higher LET has a highly non-linear relationship with the $E_{dep,i}$ [13, 17]. This means that dose alone is an insufficient measure to evaluate the true effect on tissue. We also need the LET; that is, the single particle detection sensitivity.

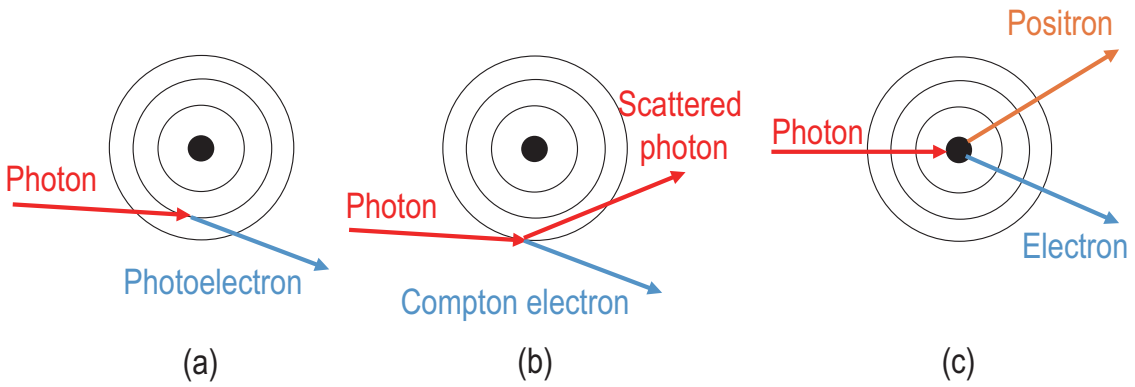

Figure 2.2: Illustration of photon interaction with an atom: (a) photoelectric effect, (b) Compton scattering, and (c) pair production.

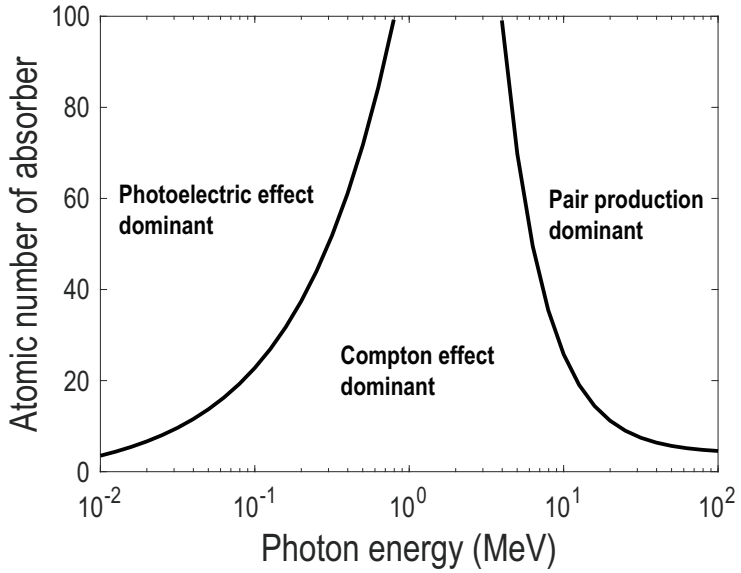

Figure 2.3: The interaction modes of photon at different absorber atomic number (adapted from [20]).

2.2 Photon Interaction with Matter

Depending on the energy, photons deposit energy in the matter in three ways: 1) photoelectric effect (photon energy <100 keV), 2) Compton scattering (all energy range), and 3) pair production (photon energy >1.022 MeV) (See Fig. 2.2) [19]. Fig. 2.3 shows the interaction

modes of photon. For example, the Compton effect is the dominant mechanism to deposit energy in the energy range between 70 keV and 14 MeV in silicon (Z = 14) [20].

The photoelectric effect is dominant at low energy. The incident photon is completely absorbed by the atom and ionizes it. The kinetic energy of the photoelectron can be expressed as

$$KE_e = E_{ph} - BE, \tag{2.3}$$

where E_{ph} is the energy of the incident photon and BE is the binding energy of the photoelectron. However, in the clinically-relevant energy range (few MeVs), the photoelectric effect is not significant.

Unlike the photoelectric effect, the photon does not disappear through the Compton scattering. The Compton electron bounces off the atom with a random direction and kinetic energy. The incident photon loses momentum and energy after the interaction. The resulting photon energy and kinetic energy from the Compton electron are

$$hv' = \frac{hv}{1 + (hv/mc^2)(1 - \cos\theta)} \tag{2.4}$$

$$T = hv\frac{1 - \cos\theta}{mc^2/hv + 1 - \cos\theta}, \tag{2.5}$$

where h is the Plank's constant, v and v' are the frequency of the incident and scattered photon, respectively, m is the electron mass, c is the speed of light, θ is the scattered angle of the photon, and T is the kinetic energy of the Compton electron [19].

Lastly, when a high energy photon collides with a nuclei, positron and electron pair are generated through the pair production. The positron is an antiparticle of the electron and has the same mass (511 keV). Any photon energy above 1.022 MeV is shared as the kinetic energy of the resulting positron-electron pair. Note that the threshold of the pair production is 1.022 MeV.

2.3 Single Charged Particle Detection using a Diode

When a charged particle interacts with a semiconductor diode, some of the energy deposited in the depletion region of the diode generates electron-hole pairs (EHPs). The average number of EHPs generated in a silicon diode is

$$EHP = \frac{LET \times t_{dep} \times qu}{\sin\theta_p \times 1.12\,\text{eV}}, \tag{2.6}$$

where LET is dE_{dep}/dx, t_{dep} is the thickness of the depletion region, θ_p is the incident angle, and qu is the quenching effect that describes approximately 1/3 of the deposited energy is used to generate EHPs. The other 2/3 is either dissipated by heat or via fast recombination of EHPs. The value 1.12 eV represents the bandgap energy of the silicon. LET is a highly

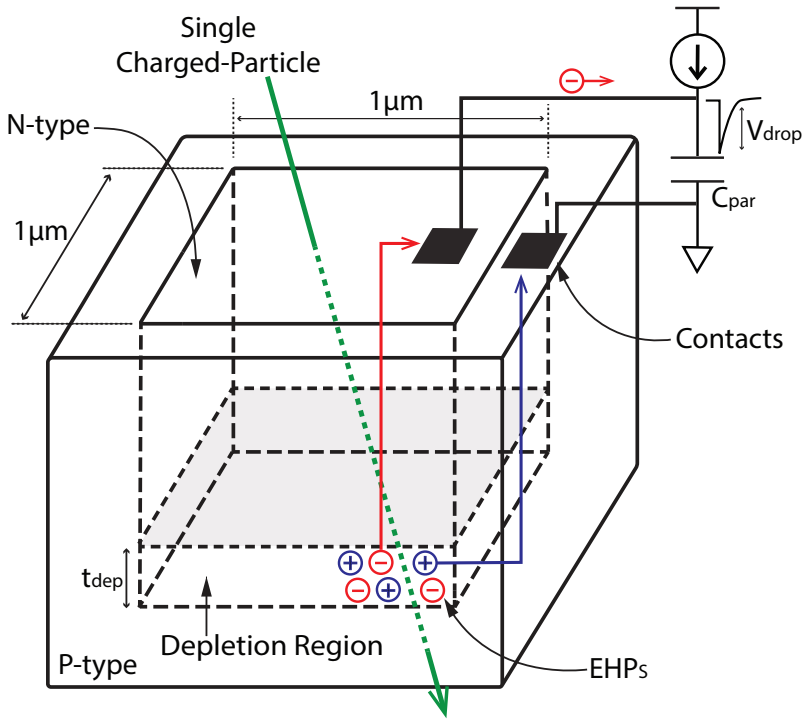

Figure 2.4: Illustration of diode sensing mechanism.

non-linear function of the incident energy. Note that, in EBRT, because the incident angle of the charged particle from the source is fixed and we know the sensor orientation, θ_p can be easily known.

Fig. 2.4 depicts the diode sensing mechanism. When the diode is reversely biased by a current source, the generated electrons move to the parasitic capacitance and create a voltage drop of

$$V_{drop} = \frac{q_e \times EHP}{C_{par}}, \tag{2.7}$$

where q_e is the charge of an electron and C_{par} is the parasitic capacitance. Therefore, to achieve single particle sensitivity, a nearly minimum size diode ($1\,\mu\text{m} \times 1\,\mu\text{m}$) is used to reduce C_{par} because, for a single particle traversing the diode, the average number of EHPs is determined mostly by fabrication parameters and charged particle energy. In order to have wide detection area, we designed diodes into arrays. When designing an array, we want to maximize the fill factor (defined as the ratio of diode area to the area of the whole circuitry) to capture as many incident particles as possible. Fig. 2.5 depicts the average voltage drop by a single proton and electron assuming C_{par} of 2.5 fF, t_{dep} of $0.1\,\mu$m, and a quenching effect of 1/3. NIST PSTAR and ESTAR table are used to calculate the LET [15, 16]. The voltage signal produced during a collision ranges from 4 mV to 78 mV at 1∼67 MeV proton energy

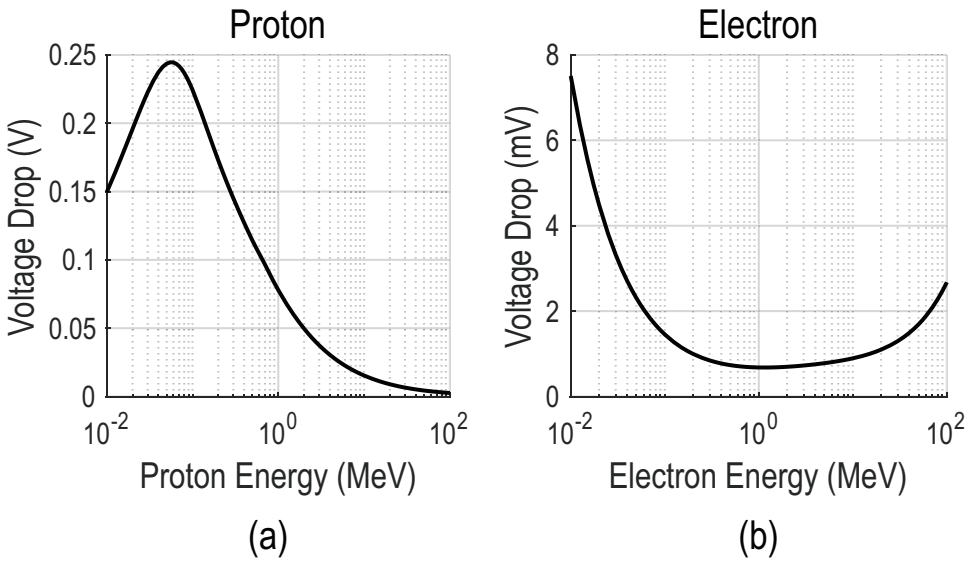

Figure 2.5: Expected average voltage drop at the diode sensing node assuming 0.1 μm depletion thickness and 2.5 fF C_{par} by (a) proton and (b) electron.

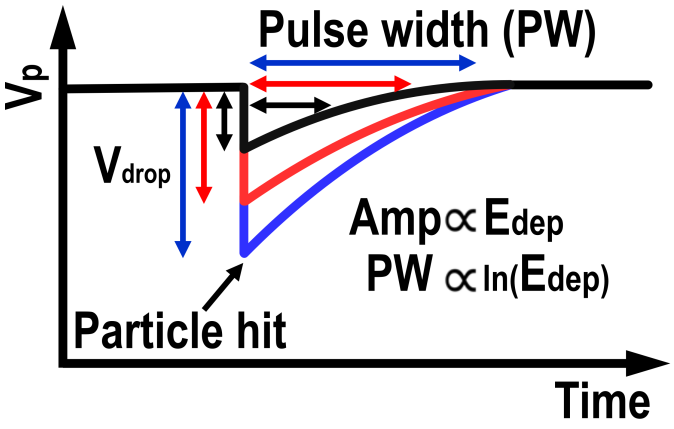

Figure 2.6: PW sensing mechanism.

range. The voltage drop is a nearly instantaneous event.

Sensing the instantaneous voltage drop generated during a collision requires high speed analog-to-digital converters (ADCs) which are power-hungry and occupy a large area (especially for an array). For example, if the time constant of the diode sensing node is 350 μs, the sampling rate of per-pixel ADC needs to be greater than 100 kHz to sample the V_{drop} with an error less than 1.5 %. Assuming 64 per-row ADCs, 6 bit resolution, and the figure-of-merit of 1.3 fJ/step [23], 64 6.4 MS/s ADCs will consume 34 μW and the total ADC area will

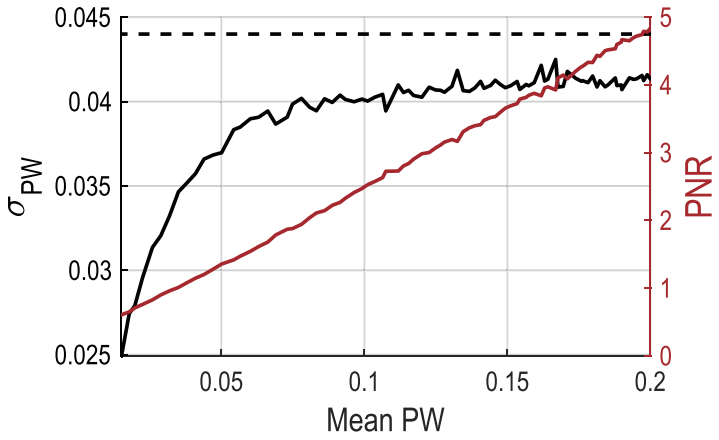

Figure 2.7: Monte Carlo simulated mean PW versus σ_{PW} and PNR.

be large. In addition, the system has to output 7.4 Gbps of data, or additional circuitry is required for post-processing, which is impractical in implantable applications. In contrast, measuring the time it takes for the generated voltage to return to its baseline is relatively straightforward. We call this delay the pulse width (PW) (See Fig. 2.6). The PW can be expressed as

$$PW = \tau \ln\left(\frac{V_{drop}}{V_{th}}\right) = \tau \ln\left(\frac{q_e \times qu \times E_{dep}}{1.12 \times \sin\theta_p \times V_{th} \times C_{par}}\right),$$

where τ is the time constant at the diode sensing node and V_{th} is the threshold voltage of detection. Even though the sensor output has a logarithmic relationship with E_{dep}, this can be pre-calibrated before use.

Including electronic noise at the diode sensing node, v_n, PW can be expressed as

$$PW = \tau \ln\left(\frac{V_{drop}}{V_{th} + \overline{v_n}}\right). \tag{2.8}$$

Given this, we can define pulse-width to noise ratio (PNR) as

$$\text{PNR} = \frac{\sqrt{\mathbb{E}[PW^2]}}{\sigma_{PW}} > \frac{\ln(V_{drop}/V_{th})}{\sigma_{v_n}/V_{th}}, \tag{2.9}$$

where the delta method is used to find the upper bound for the standard deviation of a logarithmic function. Fig. 2.7 shows the Monte Carlo simulated mean PW versus σ_{PW} and PNR. Because PNR is proportional to the mean PW, V_{drop} versus PNR is logarithmic. We can also define signal to noise ratio (SNR) as V_{drop}/σ_{v_n}. Thus, the ratio of PNR to SNR is

$$\frac{\text{PNR}}{\text{SNR}} > \frac{V_{th}\ln(V_{drop}/V_{th})}{V_{drop}}, \tag{2.10}$$

which is always less than 1. This means that the PW sensing methodology loses resolution because of the logarithmic transformation of the signal. However, SNR in this analysis assumes perfect sampling of the critical time points of V_{drop} (e.g. the time points corresponding to proton hits) which is impossible in practical situations when using an analog-to-digital converter. The actual PNR loss is subsequently expected to be less than that for the ideal situation.

Chapter 3

System Design

The design consists of a 64×64 pixel array, a main digital block, a SRAM control block, and a frequency locked loop (FLL). The system must feature low power consumption for future wireless applications, millimeter-scale size, enough detection area with sufficient fill-factor, and robustness to process mismatches.

The following sections discuss the analog pixel design, digital system design, FLL, and calibration steps.

3.1 Analog Pixel Design

Fig. 3.1 illustrates the pixel design. To reject common mode noise (i.e. 60 Hz noise or process, voltage, and temperature (PVT) variation), a differential sensing scheme is used. Two diodes, diode P and N, are grouped into one pixel unit. A P-type PN diode is used for maximizing the depletion region thickness. A nearly minimum size PMOS current source supplies current to the diode. The bias voltage of the current source (V_{bdio}) can be set to vary the depletion region thickness, time constant of the sensing node, and the DC voltage accordingly based on target beam settings. The trade-off is between the required bandwidth and the measurable proton flux range. For example, higher V_{bdio} value gives greater time constant, lower input DC voltage to the following amplifier, and smaller depletion region thickness. In our target beam setting, the time constant at the sensing node is designed to be approximately 350 μs.

The differential amplifier should feature low input capacitance, high gain, low noise, and low DC output voltage mismatch. Voltage signal at the diode sensing node decreases as the input capacitance increases. Input transistors are critical, as there is a trade-off between the input capacitance and the DC output voltage mismatch. To balance these trade-offs, low V_{th} (LVT) NMOS devices with 600 nm/600 nm are used as the input transistors. The differential amplifier occupies a 4 μm × 5.6 μm area. In addition, the differential amplifier is designed to give optimal noise figure value.

A high-pass filter with a 30 fF metal-oxide-metal capacitor (MOMCAP) is used to reject

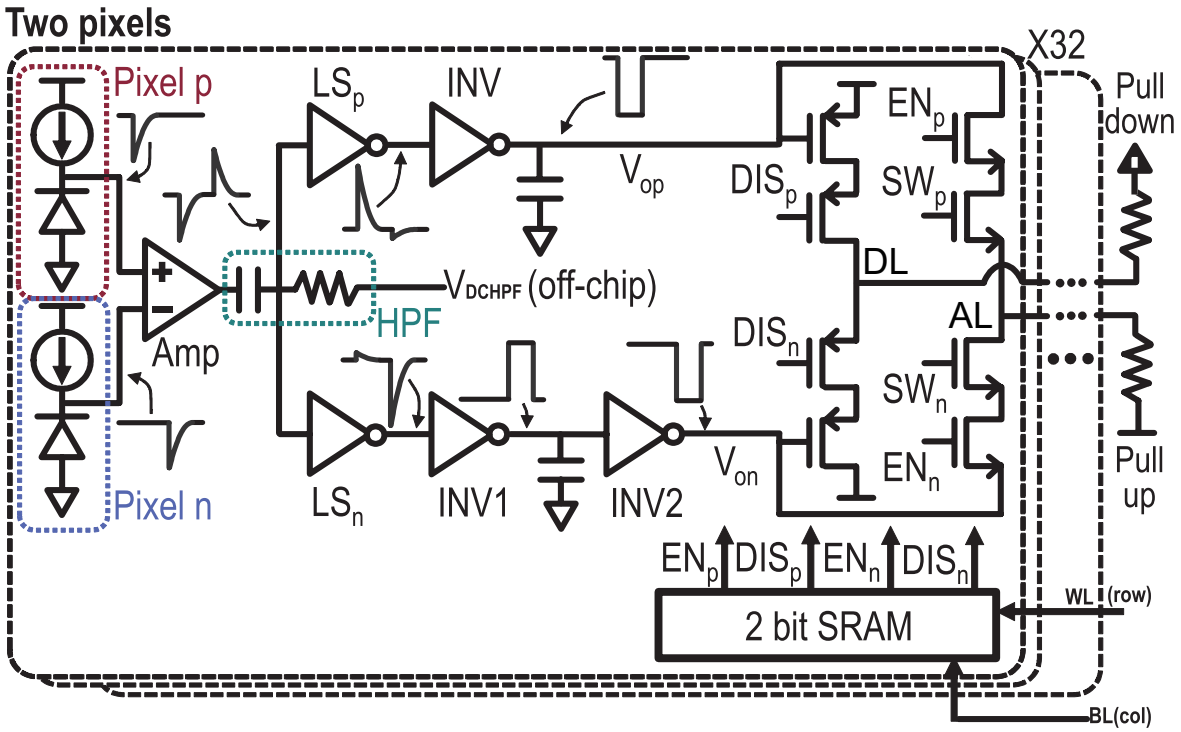

Figure 3.1: Schematic diagram of a pixel unit.

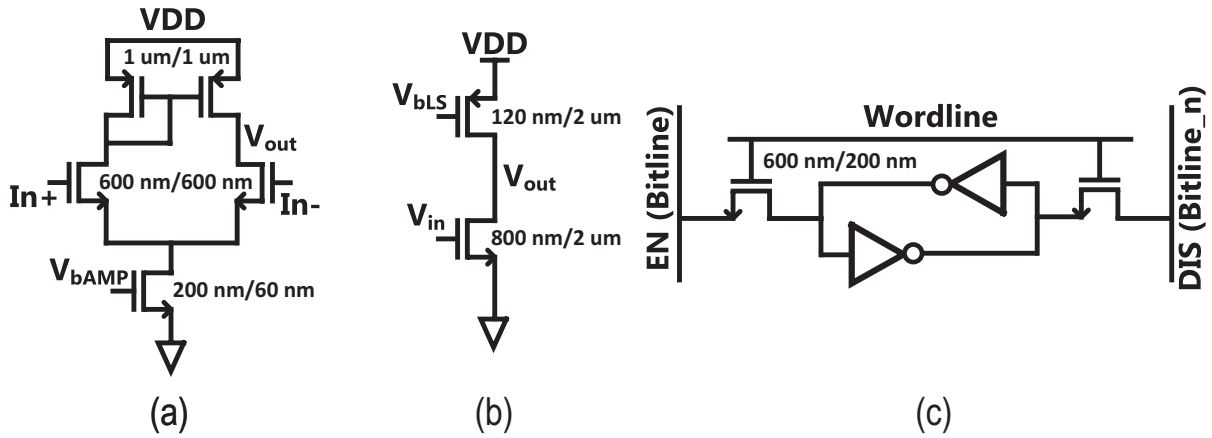

Figure 3.2: Schematic diagram of (a) differential amplifier, (b) level shifter, and (c) in-pixel SRAM.

the DC output voltage variance of the differential amplifier, and to set the DC voltage to a common voltage uniformly across all pixels by off-chip V_{DCHPF}. To provide low f_{3dB}, 9 serial pseudo-resistors are used, as the f_{3dB} accuracy is not critical. The f_{3dB} needs to be lower

than 10 Hz to ensure accurate measurement of the PW. The high-pass filter is designed to have f_{3dB} of 4.8 Hz.

The level shifters (LS) shift the DC voltage downward (LS_p) or upward (LS_n) to clip signals coming from the other diode. This enables passing signals from the corresponding diode only. The V_{bLS} is an essential variable that controls the trade-off between sensitivity of signal detection (V_{th}) and the false positive pixel rate (i.e., the ratio between the number of false positive pixels and the total number of pixels). For instance, lowering V_{bLSp} increases the output DC voltage of LS_p, leading to the triggering of the following inverter by a smaller signal. However, it also increases the chance that the noise can trigger the inverter.

Diode transient pulse is converted to a digital pulse through inverters. The output digital pulses, V_{op} and V_{on}, turn on PMOS switches to create the inverted signal on Data Line (DL), which is shared by pixels on the same row.

Due to PVT variations, there is a chance that some pixels are constitutively[1] active and output a false-positive signal even in the absence of radiation events. Because the DL is shared by pixels on the same row, these false positives would hold the DL high and block signals coming from other pixels. Therefore, an in-pixel standard 1-bit 6T SRAM block is implemented to disable any false-positive pixel. The SRAM outputs EN and DIS signals that control the final digital switches (see Fig. 3.1). Disabling these problematic pixels is called calibration and will be explained in Section 3.4.

The detailed schematics of the differential amplifier, LS, and SRAM are shown in Fig. 3.2.

The overall pixel size is $8\,\mu\text{m} \times 8\,\mu\text{m}$, leading to a fill-factor of 1/64. This means that there exists a high chance of charged particles striking the transistors. Assuming the PN junctions of the transistors have a similar depletion depth to that of the diode, this will create a voltage drop at the node with amplitude

$$V_{drop} \leq (250\,\text{mV}) \times \frac{C_{par,diode}}{C_{par,circuit}}, \tag{3.1}$$

where $C_{par,diode}$ and $C_{par,circuit}$ are the parasitic capacitances at the diode node and the node of the charged particle hit, respectively, and 250 mV is the maximum voltage drop by a proton hit (see Fig. 2.5(a)). To address this issue, we designed the pixel such that either: 1) the time constant of the node is less than the LSB of the PW sampling, which is $6\,\mu$s; or 2) $C_{par,circuit}$ is much greater than $C_{par,diode}$. For instance, the static DC current of the differential amplifier is 120 nA, and thus the worst case scenario will create a signal

$$PW = \frac{V_{drop}}{dV/dt} = \frac{250\,\text{mV} \times C_{diode}}{60\,\text{nA}} \approx 10\,\text{ns}. \tag{3.2}$$

Also, the parasitic capacitance at the HPF is more than 10 times larger than that at the diode node so that the proton hit at the HPF cannot trigger the inverter.

[1] inherently

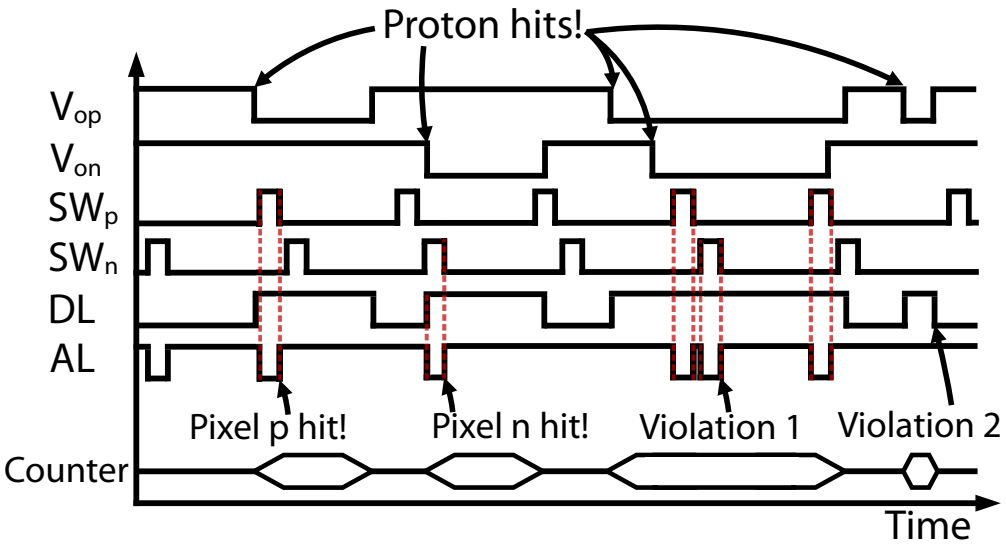

Figure 3.3: Timing diagram.

Fig. 3.3 illustrates the timing diagram. A charged particle hit at the diode creates a voltage pulse at one of the output nodes: V_{op} or V_{on}. Then, the same digital pulse but with opposite polarity is created on the DL. The PW is then quantized by a 10-bit digital counter with LSB of 6 μs. Column sweeping signals (SW_p and SW_n) are 64 non-overlapping periodic 500 ns signals generated from the main digital block. The sweeping signals are then transferred to the Address Lines (ALs), which are also shared by the pixels on the same row, when the corresponding pixel has a charged particle hit. Therefore, the main digital block can identify the column address of the proton hit by comparing the sweeping pulse and the AL signal. The sweeping lines are designed so that the overall delay it takes for the signal to travel from the main digital to the pixel and back does not exceed 500 ns.

Note that this design methodology cannot distinguish multiple charged particle hits at different pixels on the same row. This event creates the DL pulse that is the logical OR operation of two voltage output pulses, making the DL pulses inseparable. However, such an event can be easily identified because more than two sweeping pulses will be transferred onto the AL during a single DL signal (See Violation 1 in Fig. 3.3). If there are more than two column addresses in a single DL pulse, the main digital block triggers violation 1 to the corresponding data. We can simply discard these events because: 1) this is a rare event; and 2) discarding them will not change the overall statistics because this is a purely stochastic event. Also, the DL PW must be greater than 500 ns $\times$ 64 = 32 μs to guarantee that the column address is accurately identified. If not, there exists a chance that the column address is missing (See Violation 2 in Fig. 3.3). Two types of events, the multiple hit event and the address missing event, are called violation events, and we discard them. The multiple hit violations can be reduced by decreasing the time constant of the diode sensing node. However, this increases the overall power consumption because the 10-bit counter must

Table 3.1: Internal clock configurations

	Configuration	Default Value	Min	Max
t_{mst}	0.1, 0.125, 0.25, 0.5, 1 μs	0.125 μs	0.1 μs	1 μs
t_{cnt}	t_{mst}×16, 32, 48, 64, 128	6 μs	1.6 μs	128 μs
t_{addr}	t_{mst}×2, 4, 8, 32	0.5 μs	0.2 μs	32 μs
t_{PISO}	t_{mst}×1, 2, 4, 8	0.5 μs	0.1 μs	8 μs
t_{SRAM}	t_{mst}×1, 8, 32, 64	1 μs	0.1 μs	64 μs

count faster. We can also mitigate the address missing violations by sweeping the columns faster. Nevertheless, this might result in addressing the wrong columns, as the overall delay of the sweeping signal can exceed its pulse width. Note that the charged particle hit count can be retrieved even when violation events occur.

A key advantage of our method is that the pixels consume only static power in the absence of radiation. Unlike traditional imaging applications where every pixel captures the signal periodically, only the struck pixel captures the signal and consumes dynamic power. This is made possible by the PW sensing strategy, and would not be true of a voltage sensing scheme.

In addition, depending on the energy and type of incident charged particle, the user can tune the chip accordingly by adjusting pixel bias voltages. For example, when measuring electrons, which deposits much smaller energy than heavier particle, V_{bdio} can be increased to make the time constant bigger. Also, decreasing V_{bLSp} and increasing V_{bLSn} help capture smaller signals.

3.2 Digital System Design

Fig. 3.4 illustrates the overall system. The main digital block features the acquisition of the DL and AL signals, collecting them and buffering, and configuring internal parameters. The SRAM control block manages the enabling and disabling of pixels, as well as the reading of current SRAM values.

The DL and AL lines on each row have pull-down and pull-up transistors, respectively. The 10-bit counter starts counting at the rising edge of the DL signal. The reason why 10-bit resolution is needed is that signals with small PW need to be captured, as it would help more accurately measure the statistics. During counting, the addressing block stores the current SW_{idx} value when the AL is high. The counting is finished at the falling edge; and the 10-bit counter value, 6-bit row address, 6-bit column address, and 2-bit status (00 : valid, 01: multiple proton hit, 10 : column address missing) are transferred to the first-in-first-out (FIFO) block.

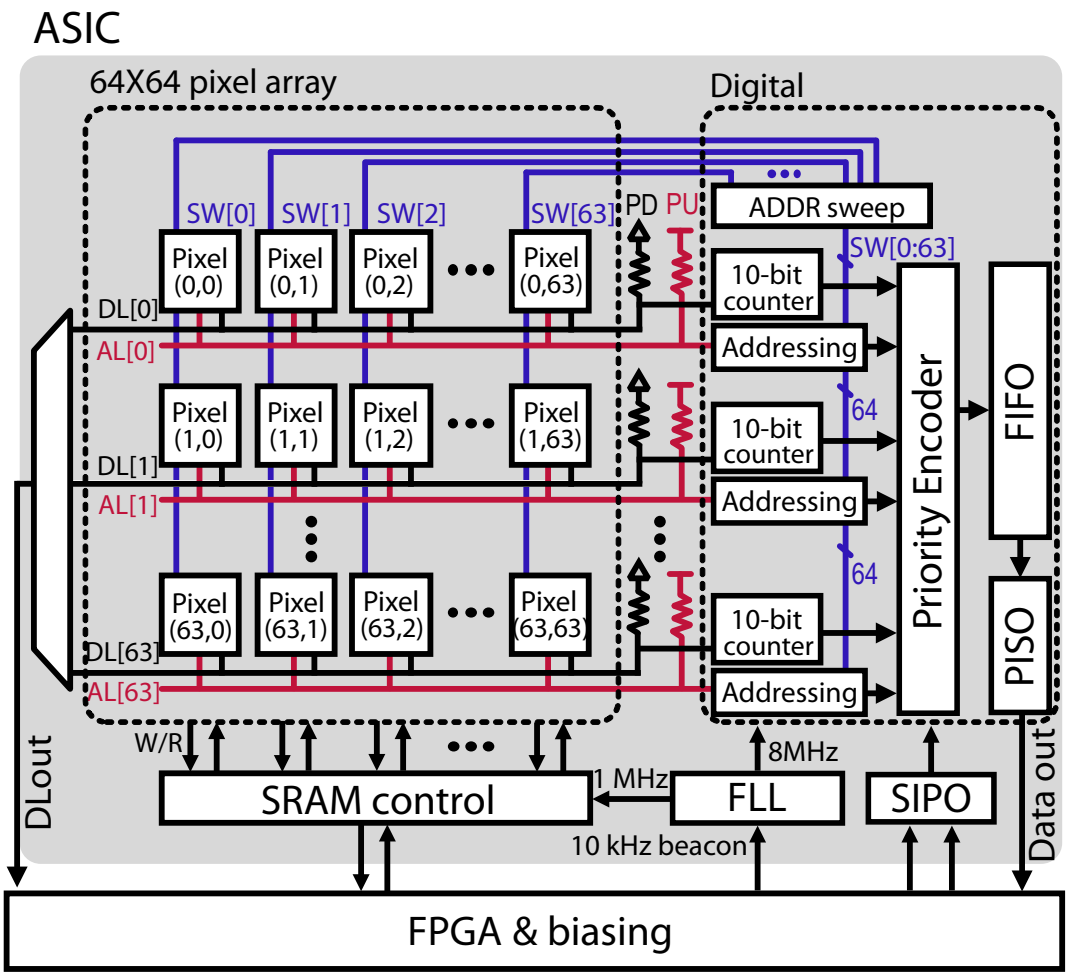

Figure 3.4: Overall system diagram.

When multiple rows have data, the priority encoder selects a row that has data and the highest priority. The rows range from 0 to 63, and a lower number translates to higher priority. This prevents data congestion at the interface between the 64 row blocks and the FIFO. The FIFO block has a width of 24 bits and depth of 16. The FIFO stores the data only when there is a particle hit. The maximum particle flux that the FIFO can handle is $1.67 \times 10^5 \#/s$, which is much higher than the clinical range. Finally, a parallel-in serial-out (PISO) block receives the data from the FIFO and outputs each data to off-chip.

The maximum latency happens when all rows have data ready and the FIFO is full. Therefore, the best and worst case latency can be expressed as

$$t_{latency,min} \approx PW + t_{cnt} + t_{FIFO} + 48t_{PISO}$$
$$t_{latency,max} \approx PW + t_{cnt} + t_{FIFO} + 48(16 + 64)t_{PISO},$$

where PW is the pulse width of the data and t_{cnt}, t_{FIFO}, and t_{PISO} are the clock periods of the

counter, FIFO, and PISO, respectively. In default settings, $t_{latency}$ ranges from $PW + 36\,\mu$s to $PW + 1932\,\mu$s. Also, since the PISO block is the bottleneck in transferring data, the maximum proton flux that the digital block can handle is about 41,000 particles per second, which is about 7 times larger than the expected flux in the clinical range.

To give more flexibility of operation, internal parameters can be configured through the serial-in parallel-out (SIPO) from off-chip. t_{mst}, t_{addr}, and t_{SRAM}, which are the periods of the main clock, the addressing clock, and SRAM clock, respectively, as well as t_{cnt} and t_{PISO} can be configured as shown in Table 3.1.

3.3 Frequency Locked Loop (FLL) Design

All internal digital clocks are generated from an on-chip FLL. The FLL obviates the need for external bulky crystal oscillators [27]. A 10 kHz beacon signal is sent from off-chip, and the FLL counts the digitally-controlled oscillator (DCO) clock during each period of the beacon signal. DCO frequency is adjusted through negative feedback based on the difference between the desired number of clocks in one period and the actual counter value. This enables the generation of a 1∼10 MHz main digital clock with approximately 280 kHz frequency resolution.

3.4 Calibration

The aforementioned constitutively active pixels are disabled before radiation through calibration steps. Each DL can be monitored off-chip through a 64 to 1 multiplexer. The calibration steps are: 1) disable every pixel through the in-pixel SRAM; 2) enable one pixel and monitor the corresponding DL signal for 50 ms; 3) disable the pixel if the DL signal is noisy or high; and 4) repeat this process for the remaining pixels. This calibration process is carried out by an external FPGA, and takes approximately 5 minutes.

By using this technique, we can indirectly measure the statistics of mismatch among pixels. Fig. 3.5(a) depicts the function $f_p(V_{bLSp})$ and $f_n(V_{bLSn})$. The percentage of enabled pixels after the calibration, EN, will be varied based on $V_{bLSp,n}$ value. EN is essentially the percentage of pixels whose $V_{op,n}$ is VDD, which can be described as

$$\text{EN} := 100 \sum_{i=1}^{N} 1\{V_{op,n} = VDD\}/N = \mathbb{E}[1\{V_{op,n} = VDD\}],$$

where N is the total number of pixels and $V_{op,n}$ means V_{op} or V_{on}. Fig. 3.5(b) shows the measured EN after the calibration when V_{bLSp} and V_{bLSn} are swept from 900 mV to 1100 mV. The slope from 975 mV to 1025 mV represents the mismatch of the function $V_{op,n} = f_{p,n}(V_{bLSp,n})$ among the pixels. For instance, if the pixels were identical without any mismatch, the slope would be infinite because every pixel becomes enabled at a certain $V_{bLSp,n}$ value; that is, the graph shows the measured cumulative distribution function of $f_{p,n}$.

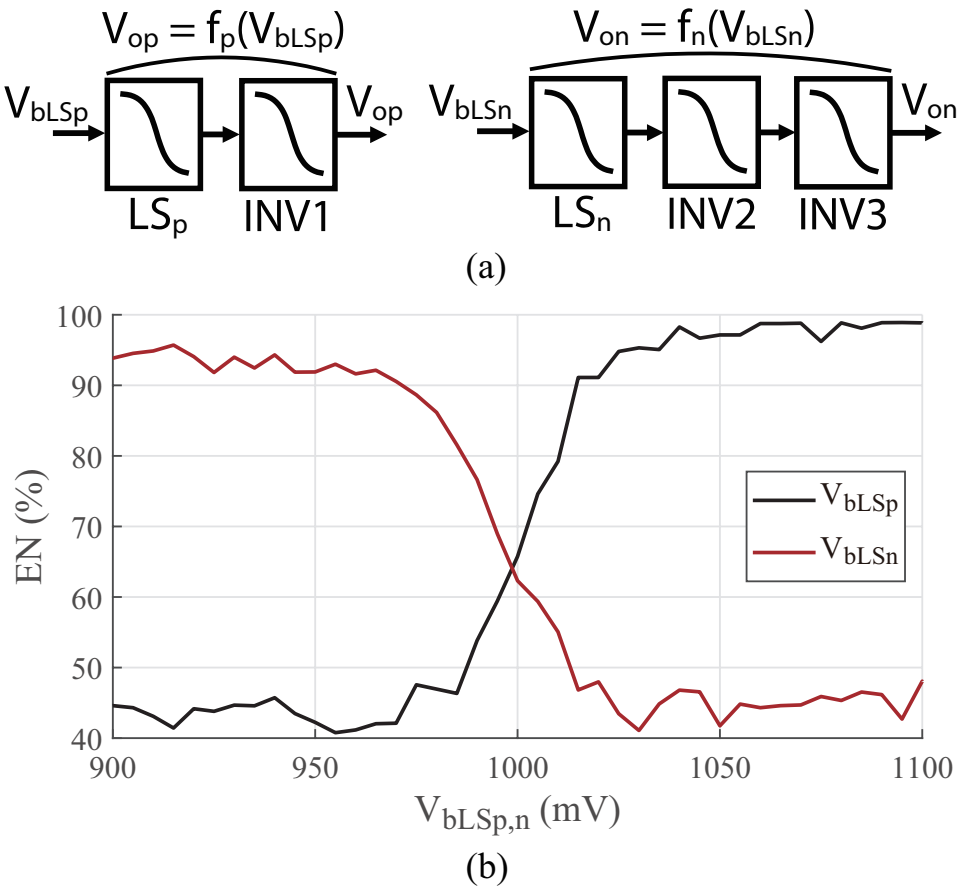

Figure 3.5: (a) Illustrations of $f_p(V_{bLSp})$ and $f_n(V_{bLSn})$ and (b) measured percentage of enabled pixels versus V_{bLSp} and V_{bLSn}. $V_{bLSp,n}$ means V_{bLSp} or V_{bLSn}.

First-order Gaussian fitting of the derivatives of the graphs gives the means of 1000 mV and 995 mV and the standard deviations of 19.33 mV and 21.85 mV for $f_p(V_{bLSp})$ and $f_n(V_{bLSn})$, respectively. Note that this is the DC offset at the LS's input caused by PVT variations at the diodes, differential amplifier, HPF, and LS. As a result, the input referred offset, at the diode sensing node, is ∼3 mV.

3.5 Chip Fabrication

A prototype single charged particle dosimeter system was fabricated in TSMC 65 nm Low-power CMOS technology. The ASIC is 940 μm×960 μm and its die photo is shown in Fig. 3.6. The detection area is 512 μm×512 μm with fill factor of 1/64. SRAM control block consists of digital communication with off-chip and SRAM read/write block.

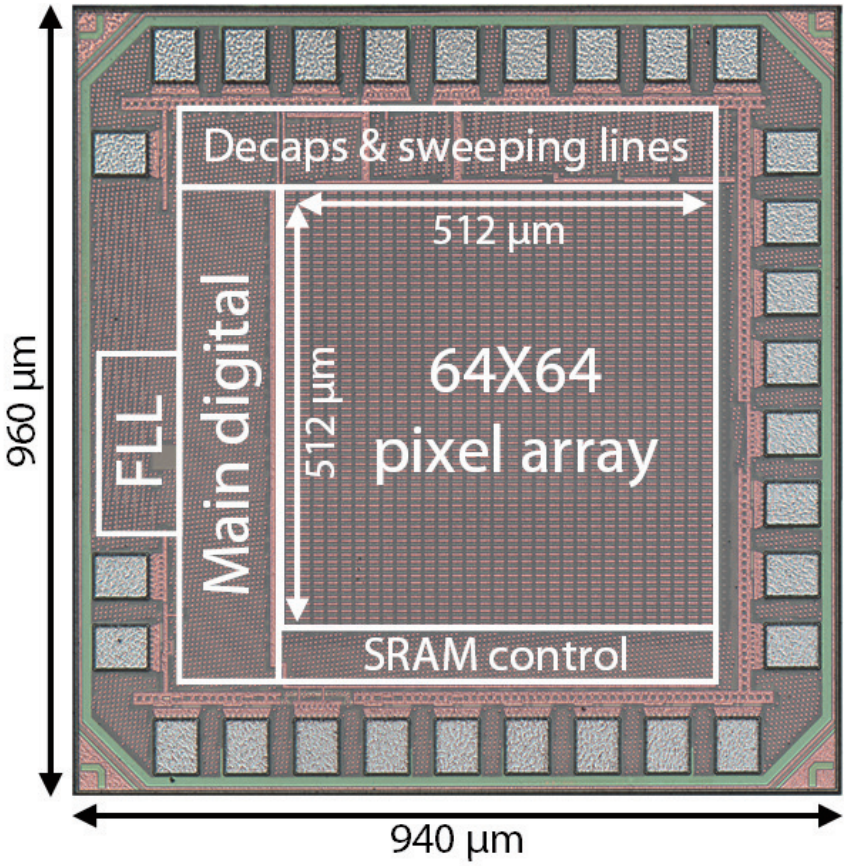

Figure 3.6: Chip die photo.

Each pixel contains two diodes with identical layout. To block unnecessary light, dummy metal layer 7 and 8 blocks are placed on each diode. The metal traces that convey digital signal (i.e. sweeping line, DL, and AL) are carefully designed in layout to minimize the interference due to parasitic capacitance.

The main digital block is designed and synthesized using Synopsys's DC and ICC software. MOMCAP and metal-insulator-metal capacitor (MIMCAP) are placed in any remaining area to reduce supply noise. Most pads are for testing and voltage biasing. Note that the number of pads can be greatly reduced by placing on-chip voltage biasing circuitry in the future design.

3.6 Motherboard and GUI Design

To provide supply and bias voltages and communicate with PC, FR-4 motherboard printed circuit board (PCB) is designed. The chip is bonded on the PCB by using silver-epoxy. The

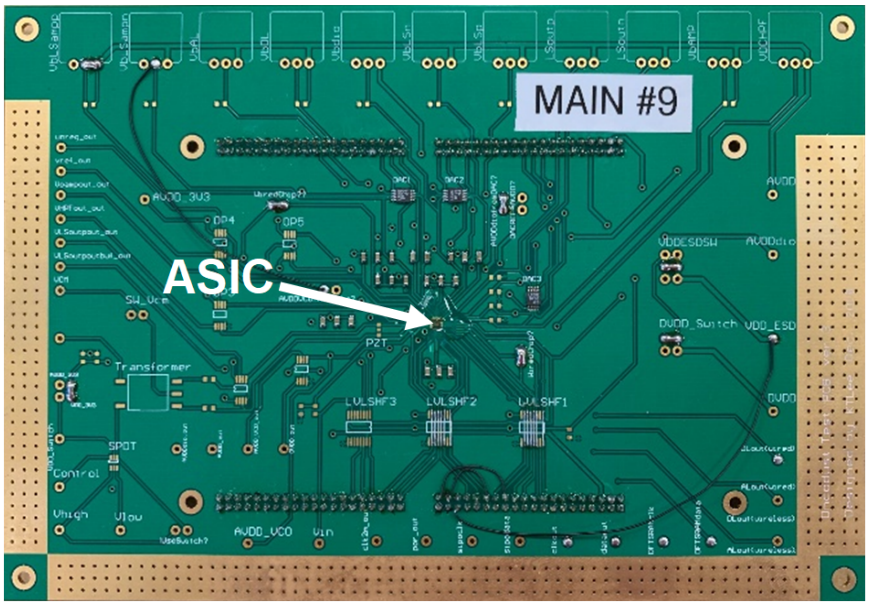

Figure 3.7: PCB photo.

pads are connected to pads on the PCB by 50 μm diameter aluminium wirebonding. Ultra-violet (UV) curable epoxy is applied to protect the bonding wires. To reduce dead-layer on the pixel array, the epoxy does not cover the sensing area.

10-bit digital-to-analog converters (DAC, Analog Devices LTC2634) provide analog bias voltages to the chip. A field-programmable gate array (FPGA, Opal Kelly XEM6310-LX45), mounted on PCB, is used to communicate between the chip and PC. FPGA also monitors the status of FLL and FIFO.

The PC communicates with FPGA through a USB cable. A python coded graphic user interface (GUI) program displays the status of the chip and statistics of the recorded data. The user can set bias and supply voltages, digital configurations, and digital clock frequency through the GUI. Fig. 3.7 shows the photo of the PCB.

Chapter 4

Measurement Results

This chapter presents measurement setups and results including electrical and using radiation producing machines (proton, beta-particle, and X-ray).

4.1 Electrical Measurement Results

Fig. 4.1 depicts the electrical measurement setup. The diode node does not have a monitoring node in current design, as placing a measurement node on the main chip would add significant parasitic capacitance and reduce the gain. Therefore, a separate 16×16 pixel testing chip with identical pixel design but with an electrical input (M1) to mimic the radiation was used to characterize noise and pixel-to-pixel variations. The M1 is a nearly minimum size transistor, 200 nm/60 nm, to minimize additional parasitic capacitance at the diode sensing node. The function generator generates 5,000 identical pulses with 1 μs pulse width. These pulses cause an instantaneous voltage drop at the diode node; the rest of the pixel circuitry outputs digital pulses on the DL. The mean and standard deviation of the PW were then measured. These measurements were repeated for various amplitude values of the input

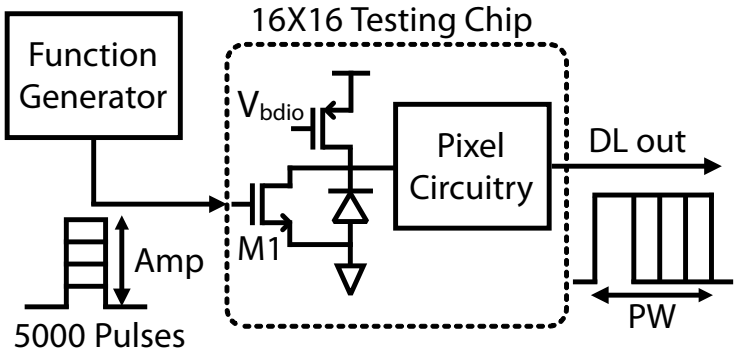

Figure 4.1: Electrical measurement setup diagram.

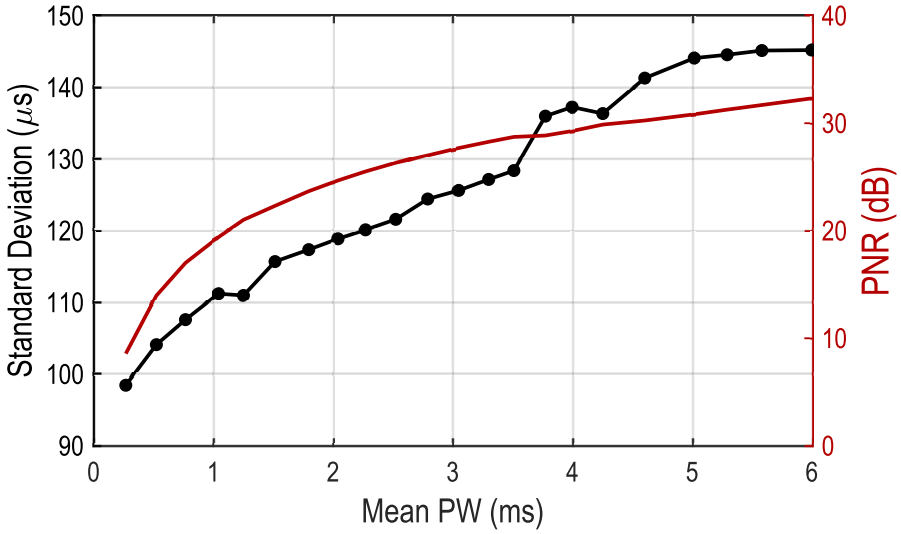

Figure 4.2: Single pixel noise measurement result.

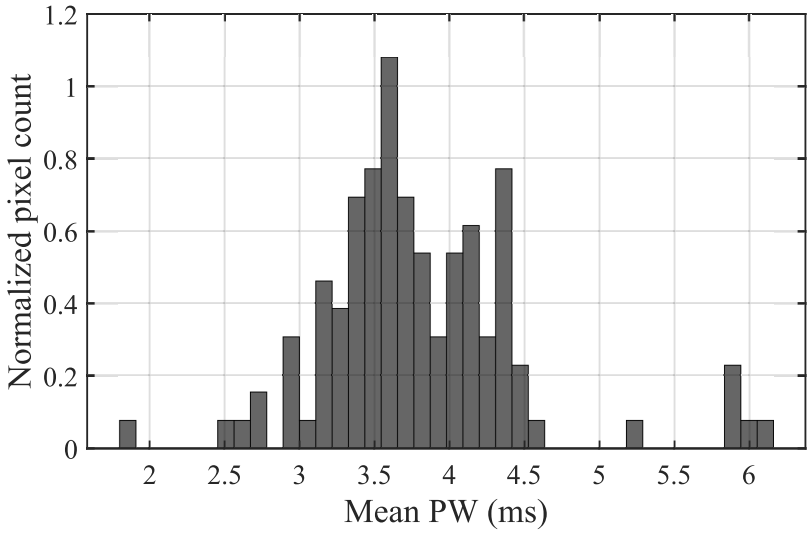

Figure 4.3: Pixel to pixel mismatch measurement result.

pulses.

Fig. 4.2 shows the single pixel measurement results. The PW variation increases with the mean PW, and the standard deviation of the PW signals is less than 150 μs throughout the whole operating range (0-6 ms). PNR is 27.7 dB at 3 ms PW. As expected from the Monte Carlo simulation result (See Fig. 2.7), the PNR has a logarithmic relationship with the Mean

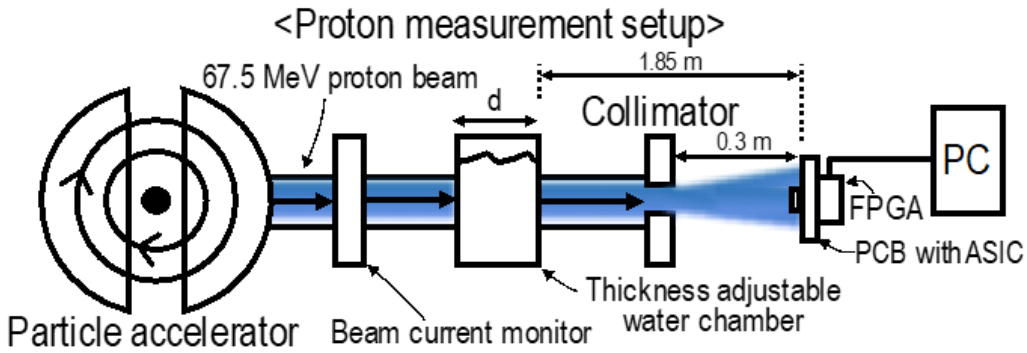

Figure 4.4: Proton measurement setup diagram at CNL.

PW. Even though the standard deviation is larger than the least significant bit (LSB, 6 μs), fast sampling is preferable to capture small pulses and to average out the electrical noise. As will be shown in the proton measurement results, the uncertainty from energy deposition by charged particle is larger than the electrical noise.

To measure pixel-to-pixel variation, 5,000 identical pulses were presented to pixels and mean PWs were measured. Fig. 4.3 is the normalized histogram of mean PWs of the 256 pixels. This histogram is essentially the input-to-output PW gain mismatch among the pixels. The variation is mainly due to the mismatch in the differential amplifier and the LS. Note that because the input transistor (M1) mismatch, which is expected to be significant due to small size, is embedded in the measurement result, the actual pixel-to-pixel variation would be smaller. In applications where high-spatial resolution dose map is required, this variation can be pre-calibrated before the treatment by measuring each pixel's responses at different charged particle energies.

4.2 Proton Measurement Results

The prototype ASIC was tested at the proton beam facility in Crocker Nuclear Laboratory (CNL) at University of California, Davis, which has treated more than 1,700 ocular patients with malignant and benign ocular tumors since 1994 [24–26]. To assess sensor performance under clinically relevant conditions, the experiment was conducted in the treating room using similar beam settings that are used for patients.

Fig. 4.4 depicts a simplified diagram of the proton measurement setup in an eye-treatment room. A 67.5 MeV with 1.3 MeV full width half maximum (FWHM) proton beam is generated by the 76-inch cyclotron. The beam enters the treatment room and passes through: ionization chamber 1 which monitors the dose; a thickness adjustable water chamber that attenuates the proton beam energy; ionization chamber 2; a patient shield; and lastly a collimator. The ASIC was placed at the position of the patient's eye during treatment (the

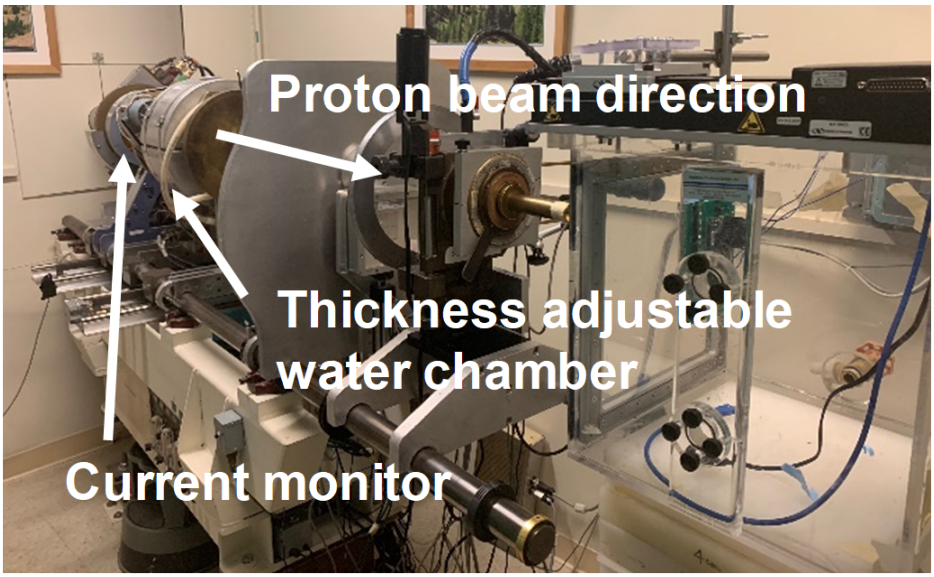

Figure 4.5: Proton measurement setup photo at CNL.

Water Thickness (d)	**Increase**
Proton energy loss in the water chamber	Increase
Proton energy after the water chamber	Decrease
Proton energy deposition in the detector	Increase
Proton flux at the detector	Decrease

Table 4.1: Relationship between the water thickness (d in Fig. 4.4) and the beam characteristics.

iso-center) and the data was collected via an FPGA. The beam energy at the patient was controlled by the water chamber. Due to the nature of the energy loss mechanism of the charged particle (Eq. (2.1)), the energy deposition by protons has an inverse relationship with the proton energy above ~0.1 MeV, thus EHP increases with increasing water thickness. Also, as the water thickness increases, the beam scatters more and thus fewer protons reach the detector. This leads to a smaller proton flux, which is the number of protons in unit area per second, at the detector. These relationships are summarized in Table 4.1

Fig. 4.6 shows measured proton flux and violation rate at different proton beam current settings. The raw beam current is proportional to the actual proton flux. The measured flux increases linearly from 0.1 nA to 3 nA, and starts to saturate after 3 nA. Even though

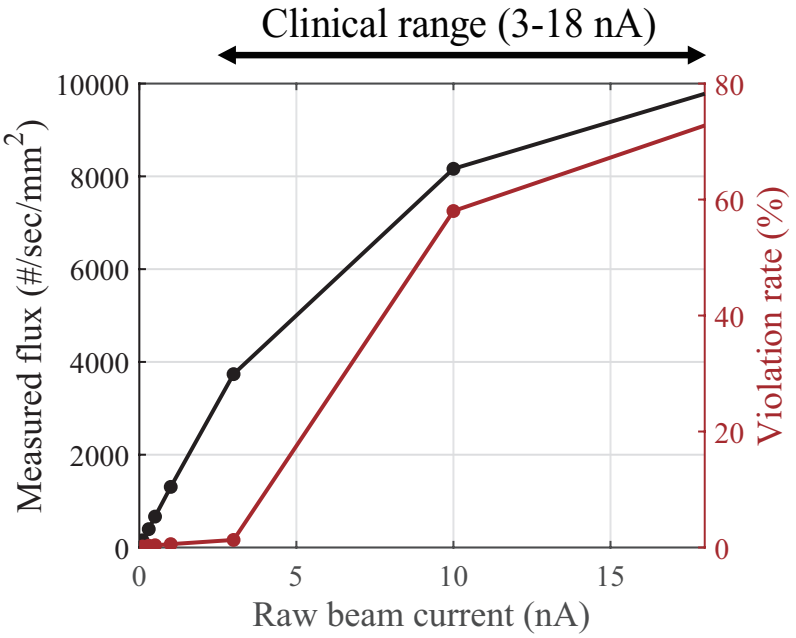

Figure 4.6: Proton beam current versus measured flux and violation rate.

the clinical range at CNL is from 3 nA to 18 nA, the remaining valid data provides enough data to extract meaningful statistics of energy deposition. We can also decrease the time constant at the diode sensing node to reduce the chance of having violations.

Normalized PW histograms measured for 80 seconds of the beam time at different water thicknesses are shown in Fig. 4.7. The 10-bit counter quantized the PW of the DL signals from 0-6138 μs with 6 μs resolution. Any DL signal whose PW is more than 6138 μs is considered to be saturated. The total proton count decreases as the water thickness increases, mainly due to the proton scattering in the water chamber. As expected, the mean PW, which indirectly measures the mean energy deposition in the depletion region, increases as the water becomes thicker.

At d = 0 mm, the measured standard deviation is 502 μs. This consists of the Landau effect, the energy distribution of the incident proton beam, the electrical noise, the pixel-to-pixel variation, and the quantization noise. From the electrical measurement result shown in Fig. 4.2, the electrical noise contributes less than 9 % to the total uncertainty.

To verify the proton measurement data, the Tool for Particle Simulation (TOPAS) was used [29–31]. TOPAS wraps and extends the Geometry and Tracking 4 (GEANT4) Monte Carlo particle simulator. GEANT4 is an industry gold-standard for analyzing the behavior of atomic particles [32–34]. Fig. 4.8 shows the measured total number of protons, mean PW, and summation of PW over a 80-second window. The TOPAS simulated total number of protons, mean energy deposition (average energy deposited by each proton), and total energy deposition for all protons, assuming a depletion region thickness of 0.1 μm, is also

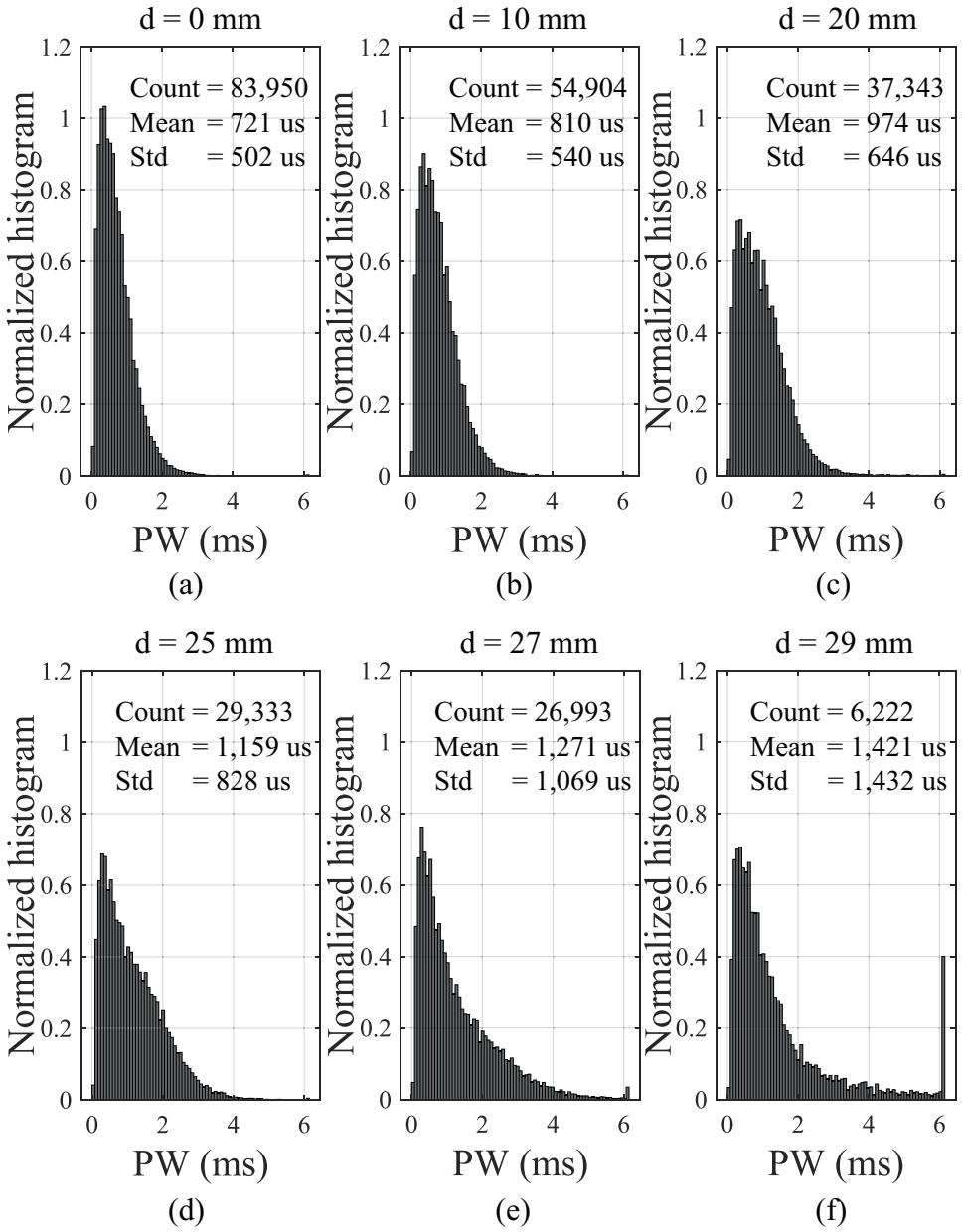

Figure 4.7: Normalized PW histograms measured for 80 seconds at (a) d = 0 mm, (b) d = 10 mm, (c) d = 20 mm, (d) d = 25 mm, (e) d = 27 mm, and (f) d = 29 mm.

shown for comparison. The trends match well with each other, and we can plot the measured mean PW (black graph in Fig. 4.8(b)) in the x-axis and the TOPAS simulated mean energy deposition (red graph in Fig. 4.8(b)) in the y-axis to show the energy deposition versus PW relationship (see Fig. 4.9). As expected from Eq. 2.8, these have a logarithmic relationship.

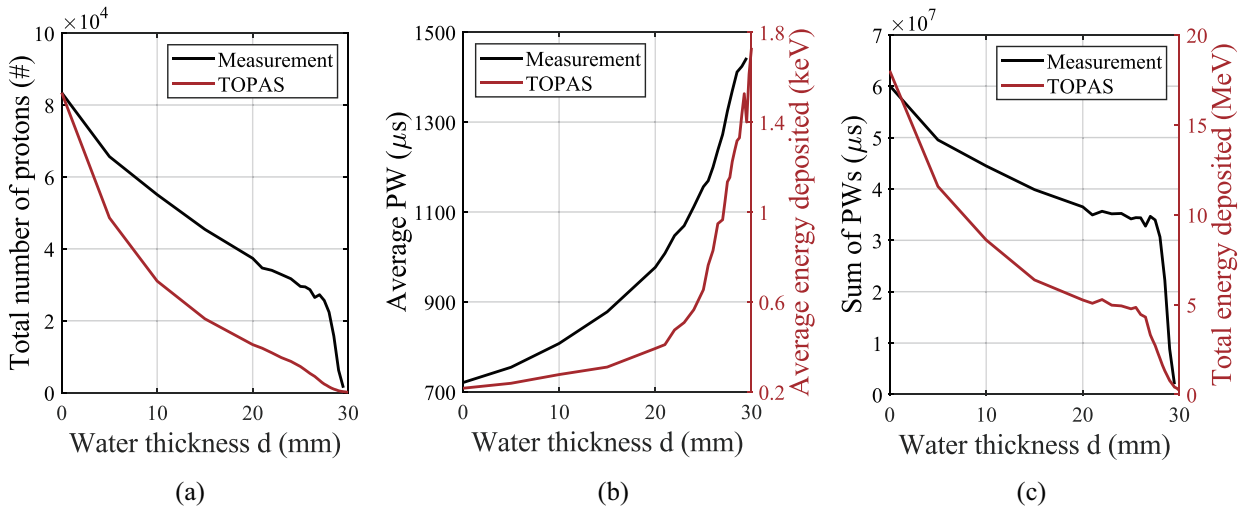

Figure 4.8: Measured and TOPAS simulated (a) total number of protons, (b) average PW (measurement) and energy deposition (simulation), and (c) summation of PW (measurement) and total energy deposited (simulation). Measurements are from 80 seconds of proton beam time. The total number of protons in TOPAS simulation is normalized to match the measured result at d = 0 mm.

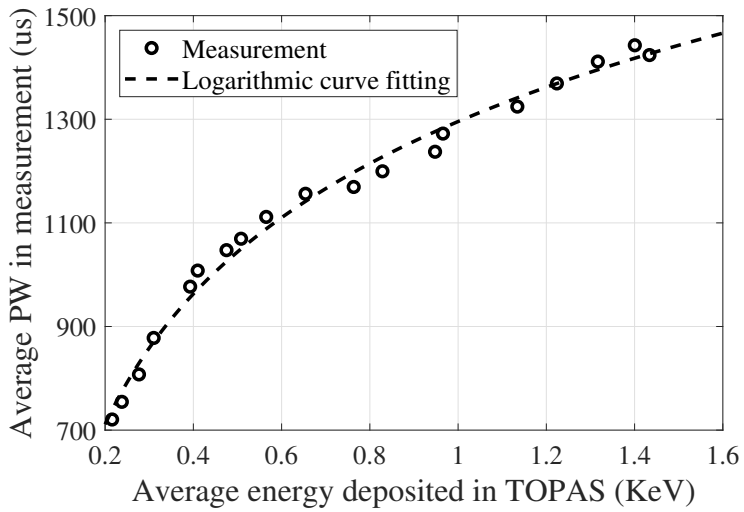

Figure 4.9: TOPAS simulated average energy deposition versus measured average PW.

The time constant at the diode sensing node is estimated to be 363 μs from a curve fit of the data.

4.3 Proton Measurement Results (In the Water)

Protons deposit their energy while penetrating a tissue. They lose energy as it passes, and their trajectory alters due to scattering. Protons with less energy scatters more. The actual total dose (or dose rate, dose per minute) in a specific location of the tissue results from both the amount of energy deposition (LET) and the flux (number of particles passing through per unit time per unit area). To understand this, it is worthwhile to simulate how proton flux and LET changes in a water column.

Fig. 4.10 shows the TOPAS simulation setup. The proton beam with the mean energy of 67.5 MeV and beam width of 2.5 cm is applied from left to right in the diagram. A water column with a variable thickness ranging from 1.8 mm to 36.8 mm degrades the proton energy and scatters the beam. A silicon detector is placed after the water column and measures the proton passing through it. Note that the density and LET of the tissue is similar to that of the water.

Fig. 4.11 depicts the TOPAS simulation result. X-axis is the water thickness. The blue curve shows the total number of protons detects at the detector. The number of protons gradually decreases until 25 mm and rapidly drops after that mainly due to the proton scattering. On the other hand, the orange curve (average energy deposited in the detector) keeps increasing until ∼28 mm and decreases after that. This is due to the shape of the proton LET curve (See Fig. 2.1). The total energy deposited (the dotted black line), which is proportional to the dose, is simply the multiplication between the total number of particles and average energy deposited. As a result, the total energy deposited increases until ∼27 mm and collapses to zero. This is the physics behind the Bragg peak. Interestingly, even with the same dose number, the mechanism can be different. For example, the dose is the same at 25 mm and ∼27.5 mm, but they are due to large number of protons depositing small average energy and few protons depositing large average energy, respectively. Because the actual biological effect (i.e. the number of double strand breaks in DNA) is highly non-linear to the LET [13], dose is not a sufficient measure in radiotherapy. Therefore, the IVD with the

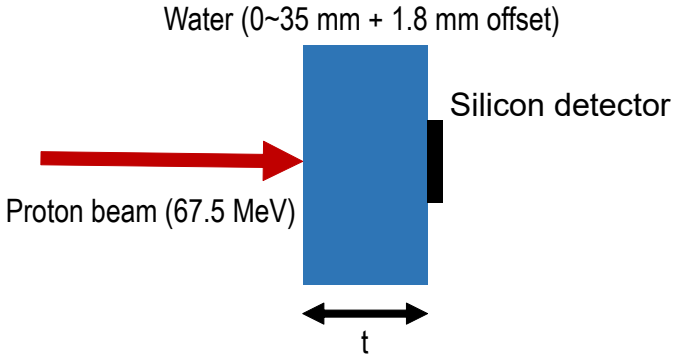

Figure 4.10: TOPAS Bragg peak simulation setup.

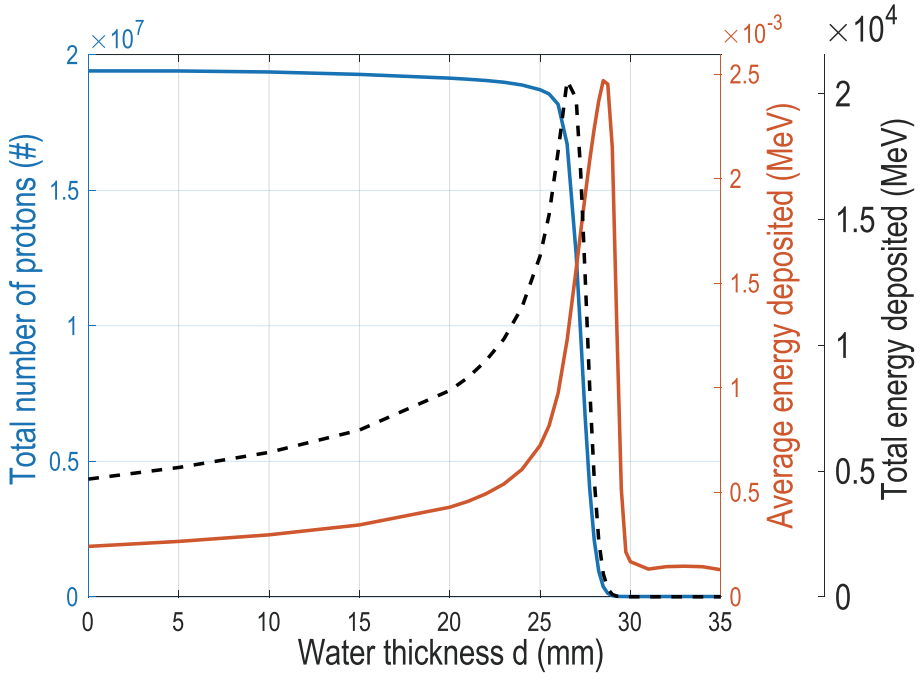

Figure 4.11: TOPAS simulated the total number of protons, mean energy deposition, and total energy deposition in the detector.

single particle sensitivity can play an important role both in clinical and research settings.

Using the same proton energy (67.5 MeV), a mouse liver with the chip implanted is radiated. The mouse liver is chosen because it is the biggest organ in a mouse and most of liver cells' division cycles are synchronized. The mouse is euthanized in an animal facility at UC Davis. The liver is then dissected. To keep the liver cells alive during the radiation, the liver is preserved in the Belzer UW Cold Storage Solution surrounded by ice to keep the organ at low temperature. Before the radiation, the liver is moved to a 25 mm × 25 mm × 25 mm polydimethylsiloxane (PDMS) box filled with the UW solution. Because the density of the PDMS (~ 0.97 g/cm^2) is very similar to that of the water, it is assumed that 2.5 mm PDMS wall behaves similarly to 2.5 mm water.

For device implantation in a mouse liver, a flexible polyimide PCB with the thickness of 0.3 mm is designed and fabricated. The polyimide PCB routes analog, power, and digital communication between the chip and the FR-4 motherboard PCB. The width of the PCB is 6 mm. Fig. 4.12 shows a microscope photo of the chip on the polyimide PCB. The backside of the chip is bonded on a ground pad using silver epoxy. The silver epoxy is cured in an oven for 15 minutes at 150 degree. Each pad on the chip is wirebonded to the PCB with 50 μm diameter Aluminium wire. To protect the wires and prevent any water contact to metal traces, UV curable epoxy coats the PCB and chip. Note that the UV curable epoxy does not cover the active area to reduce the dead layer. Because the surface of the chip is already

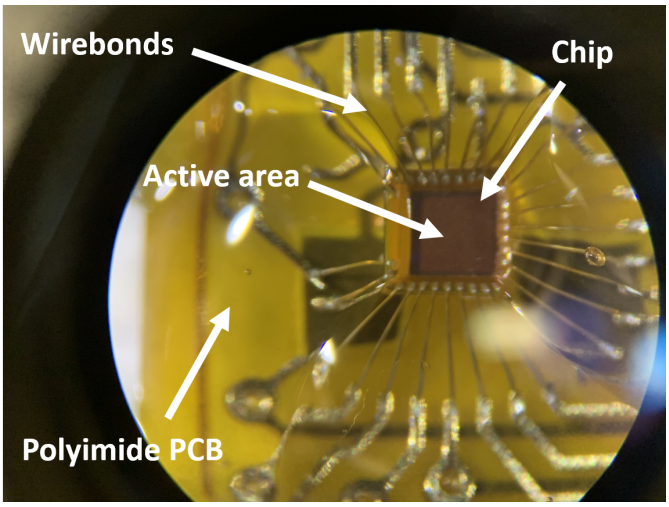

Figure 4.12: Microscope photo of the chip on the polyimide PCB.

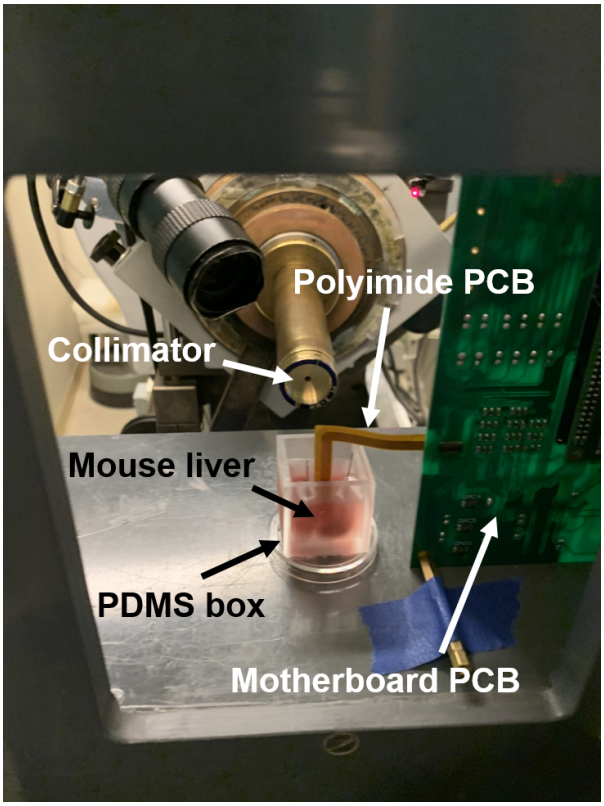

Figure 4.13: Animal experiment setup photo.

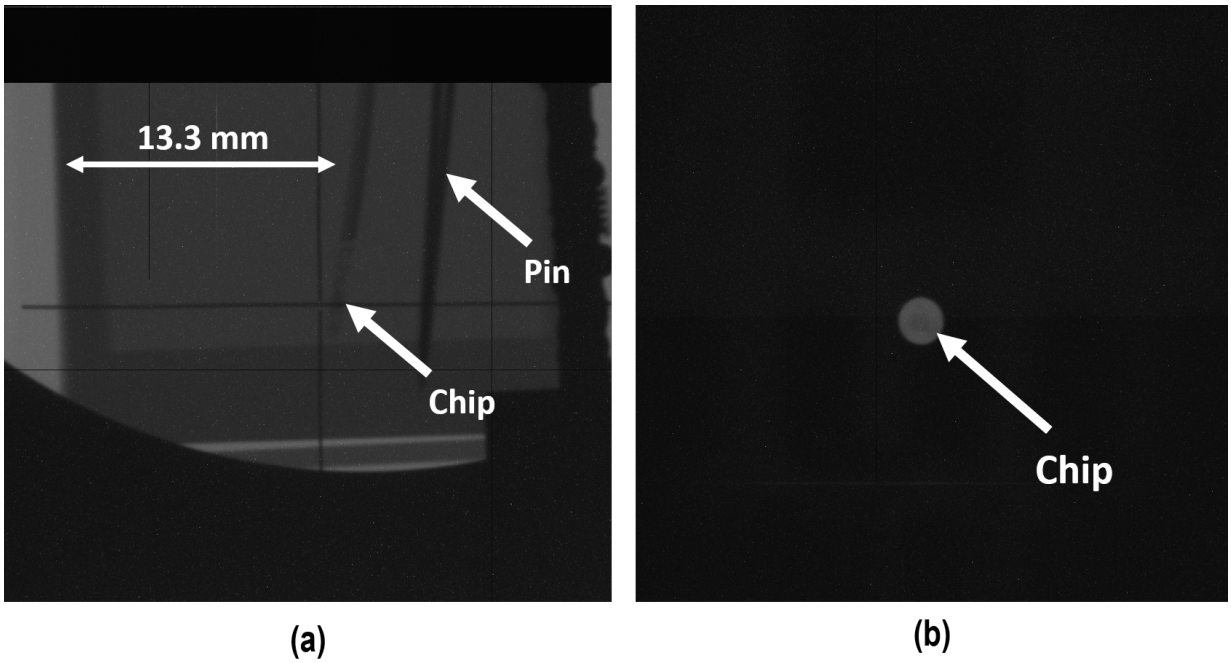

Figure 4.14: X-ray photo of the setup of (a) lateral and (b) AP view.

protected with the passivation layer, water does not affect the chip.

Fig. 4.13 shows the animal experiment setup photo. The PDMS box contains the polyimide PCB with the chip, preservation solution, and a mouse liver. Two pins hold the position of the liver. Because the pins are placed near the backside of the box, they do not affect any measurements. A 3 mm brass collimator prevents any unwanted affect on PCBs and traces by the beam.

To accurately align the beam with the device, an anterior-posterior (AP) and lateral X-ray images are used. Fig. 4.14 shows the X-ray images. The lateral X-ray camera takes an image along the axis parallel to the proton beam. The liver is not shown in the image because the X-ray mass attenuation coefficient of the liver is similar to that of the preservation solution. By using the X-ray imaging software, the distance between the wall of the PDMS box and the chip can be measured (13.3 mm). Because the Bragg peak location of the proton beam is at 28.5 mm [26], the chip is placed at the Bragg peak if there is additional water thickness of 15.2 mm, assuming the proton LET of the PDMS, water, preservation solution, and liver are the same. Fig. 4.14(b) shows the AP X-ray image. The field of view of the AP X-ray image is a 3 mm diameter circle because of the collimator. The AP image is used to precisely align the chip with the proton beam.

The thickness adjustable water chamber provides additional water with 0.1 mm resolution (See Fig. 4.4). The actual proton beam experiment consists of two steps: 1) low-dose sweeping and 2) high-dose radiation. During the low-dose sweeping, the water thickness in

Configuration		Water Column Thickness (mm)	Beam Current (nA)	Duration of Radiation (minutes)
Low-dose Sweeping	1	13.7	0.25	0.2
	2	14.2	0.25	0.2
	3	14.7	0.25	0.2
	4	15.2	0.25	0.2
	5	15.7	0.25	0.2
	6	16.2	0.25	0.2
	7	16.7	0.25	0.2
High-dose Radiation		15.2	0.25	13.32

Table 4.2: Beam configurations for the animal experiment.

the water chamber is swept with low dose. In the actual clinic, this step is to find the location of the Bragg peak. Because we know the location of the Bragg peak and the media (the PDMS box, preservation solution, and liver) is homogeneous enough, we can compare the data from the chip and the expected Bragg peak location. After the low-dose sweeping, the additional water thickness is set at 15.2 mm so that the chip is at the location of the Bragg peak. Then the beam with much higher dose is applied. For future work, the tissue imaging using an antibody that is specific to the DNA double strand breaks can be performed to verify the data.

We chose the target dose for the high-dose radiation to be 3 Gy because the tissue staining result for DNA damage saturates at the dose greater than 3 Gy. The duration of the radiation and beam current for the low-dose sweeping are carefully chosen not to damage the tissue too much. 7 nA beam current and 2.22 minutes of radiation correspond to 14 Gy peak dose in water [35]. To have 3 Gy peak dose during the high dose radiation, 0.25 nA beam current and 13.32 minutes of radiation are chosen. In order not to exceed the maximum dose of 0.3 Gy during the low dose radiation, 7 sweeps with various water thicknesses at 0.25 nA beam current and 12 seconds of radiation are performed. Table 4.2 summarizes the beam configurations.

Fig. 4.15(a) shows the measured Jacknifed means and standard deviations of PW. The blue curve represents data points of the low-dose sweepings. As expected from Fig. 4.11, the mean PW increases as the water thickness increases. This is due to having more LET as the water thickness increases around the Bragg peak ($\sim$26.5 mm). Each data set is divided into 6 groups with 2 seconds of data and the standard deviation of the mean of each group is calculated. The vertical lines at each data point represent ± 1 standard deviation. The red asterisk in the graph shows the mean PW of the high-dose radiation. The mean PW for the low-dose sweeping at 15.2 mm and high-dose radiation match well. Fig. 4.15(b) depicts the measured proton flux. The trend of the flux is similar to Fig. 4.11 around the dose peak. The proton flux decreases due to scattering. Similarly, the low-dose sweeping result

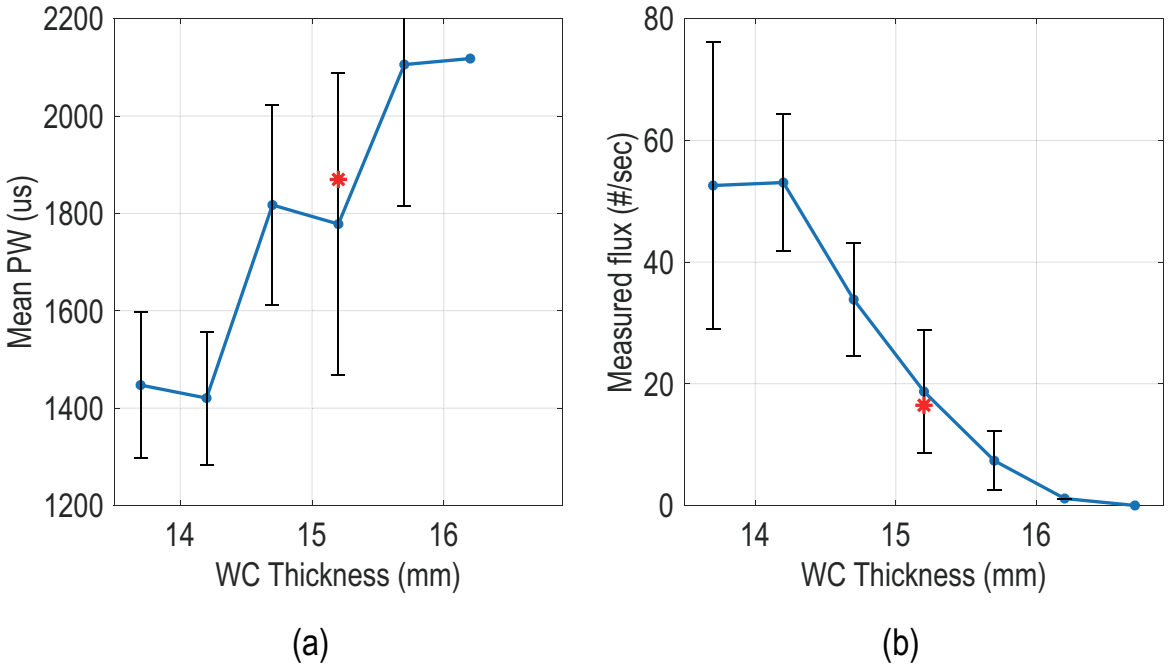

Figure 4.15: Measured mean PW and flux for the proton animal experiment.

(the blue curve) and high-dose radiation data (the red asterisk) match each other. Note that higher beam current (> 1 nA) caused an unexpected error. We hypothesize this is because protons affect the electrical characteristics of the polyimide PCB. This will be resolved if the system operates wirelessly and does not require long PCB traces.

4.4 Beta-particle Measurement Results (Linear Accelerator)

Electron beam radiotherapy has been widely used to effectively treat skin cancers and tumors near the skin. A linear accelerator generates a mono-energetic electron beam at its exit window with the energy up to MeVs. The entry dose of the 6 MeV electron beam is typically ~80 % of its maximum dose [37]. This increases as the beam energy increases. The dose becomes maximum (100 %) at z_{max} and half (50 %) at R_{50}. The electron LET in water-like tissue, averaged over the clinical energy range, is around 2 MeV/cm. The reason why the maximum dose occurs in the body (i.e. $\sim$ 2 cm for 6 MeV beam), not at the surface, is due to the scattering. As the beam penetrates, the electrons originally not situated at the primary axis of the beam scatters back to the primary axis, leading to increasing the flux at the location of the measurement. The shape of the electron depth-dose curve depends on

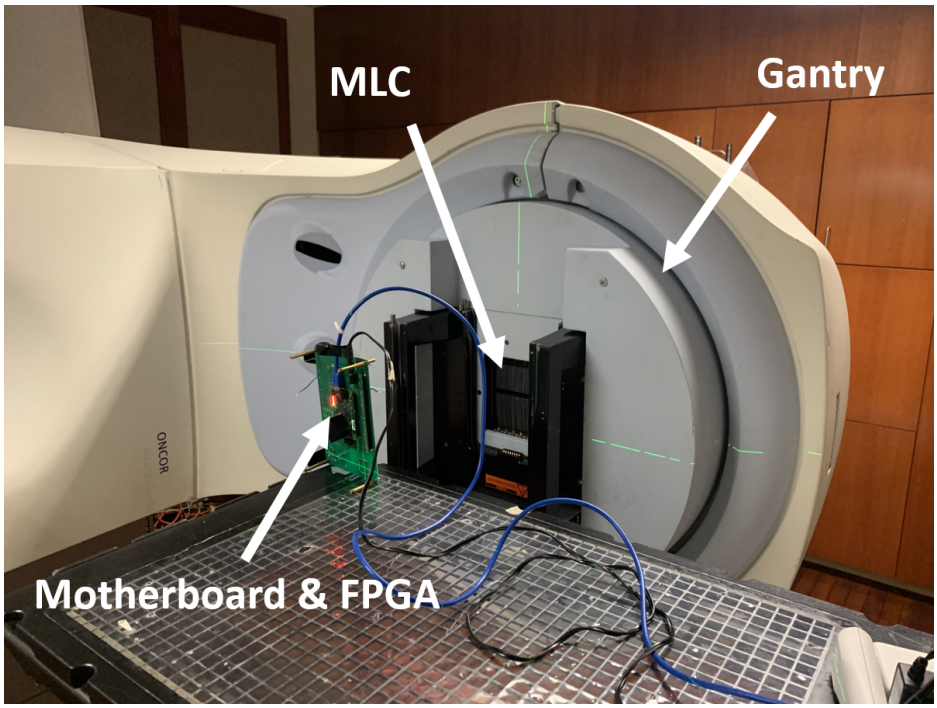

Figure 4.16: Beta particle measurement setup photo.

the machine design, beam energy, and machine accessories.

Siemens linear accelerator is used for the experiment. The machine can generate 6, 9, 12, and 15 MeV electron beams with the dose rate (Gy per minute) from 0.5 Gy/min to 4 Gy/min. The multi-leaf collimator (MLC) with 19 cm $\times$ 19 cm beam is used. Fig. 4.16 shows the beta particle measurement setup photo. The chip is placed at the isocenter using 3-axis lasers.

Fig. 4.17 shows the measured flux in counts per second at each one second time window. Total dose of 2 Gy with the dose rate of 3 Gy per minute is applied. When the beam is on, the measured flux surges to 900 #/s and becomes saturated to 400 #/s. The measured flux is zero when the machine is turned off.

Table 4.3 shows the device aging test result, where total 22 Gy of radiation is applied to the same device. The radiation causes lattice displacement in the silicon dioxide of the transistors, gradually decreasing the transistor threshold voltage linearly with the total dose deposited [35]. The violation rate, measured flux, and mean PW does not change significantly. Note that the typical total dose value during a radiotherpy is about 15 Gy.

Table 4.4 shows the measured data at different electron beam energy. Stopping power values are calculated from the silicon NIST ESTAR table [16]. The electron LET after 1 MeV increases as the energy increases, as shown in Fig. 2.1. The reason why measured flux increases as the energy increases is the electron scatters less at higher energy and as a

Experiment	Dose (Gy)	Dose rate (Gy/min)	Violation rate (%)	Measured flux (#/sec)	Mean PW (us)
1	3	300	3.96	378.57	739.45
2	3	300	3.99	436.09	735.06
3	3	300	3.74	369.26	722.24
4	3	300	3.9	442.30	731.05
5	10	300	3.89	433.78	715.7

Table 4.3: Device aging test result.

result, more electrons reach the detector. In addition, higher energy electron deposits more energy in the depletion region, leading to increasing the probability of having the voltage drop greater than the detection threshold. This also increases the violation rate at higher energy. Note that the measured flux is almost 0 when there is no beam.

To measure depth-dose curves of electron beams, water-equivalent plastic plates are used. The location of the device is changed at different water thicknesses so that the isocenter of the beam is at the edge of the water-equivalent plastics. In this way, the measurement setup is the same as moving the device in a water tank. Fig. 4.18 shows the measured total number of electrons, mean PW, and the summation of PW at different water thicknesses for 6, 9, 12, and 15 MeV electron beams. The thickness of the water is increased with 5 mm step.

In Fig. 4.18(a), the electron flux gradually increases till x_{max} (the build-up region),

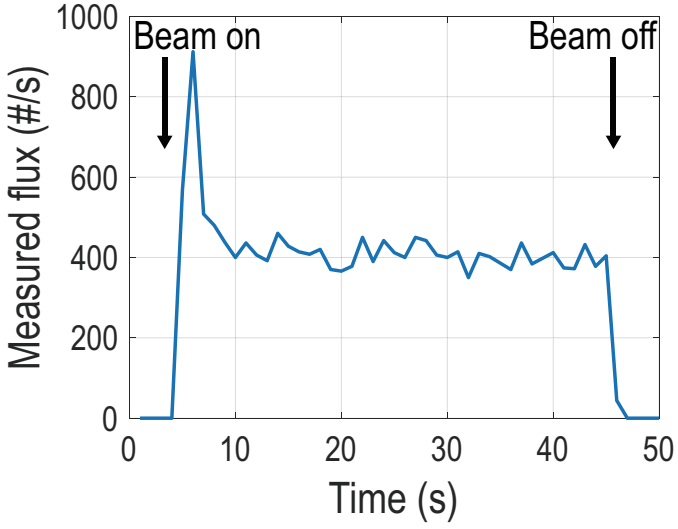

Figure 4.17: Measured flux at each time point.

Energy (MeV)	Stopping power (MeV/cm)	Violation rate (%)	Measured flux (#/sec)	Mean PW (us)
6	4.224	3.89	398.60	715.7
9	4.579	5.78	575.27	737.87
12	4.909	7.12	667.39	770.34
15	5.231	7.1	720.65	786.85
No beam			0.3	

Table 4.4: Measured data at different electron beam energy.

where the dose maximum occurs. This is due to electrons scattering back into the primary axis of the beam. After x_{max}, the measured flux rapidly decreased because most electrons are stopped and scattered out. The Bremsstrahlung tails, due to the photons created when an electron is passing by an atom and deaccelerated by the electromagnetic force (the Bremsstrahlung effect). The photon flux at the Bremsstrahlung tails increases as the beam energy increases, as higher energy electron has greater chance of producing photons by the Bremsstrahlung interactions.

The measured mean PW increases in the build-up region as the electron LET increases in the sub-MeV range (see Fig. 4.18(b)). After x_{max}, the mean PW rapidly decreases. This is because most detected electrons are due to secondary electrons produced by the Bremsstrahlung photons after x_{max}.

The Fig. 4.18(c) shows the summation of PW. Even though the summation of PW is not proportional to the dose, due to the logarithmic relationship between the energy deposition and PW, it increases monotonically as the dose increases. We can compare this with previously published results using the same machine [36]. Note that in [36], the measurement was done at much closer to the beam exit window. Clinically relevant variables are compared to verify.

- D_{surf} : percentage of the entry dose compared to the maximum dose
- z_{max} : water depth that gives the maximum dose
- R_{90} : water depth that gives 90 % of the maximum dose
- R_{50} : water depth that gives 50 % of the maximum dose
- R_{max} : water depth where the Bremsstrahlung tail starts
- D_B : percentage of dose at the Bremsstrahlung tail compared to the maximum dose

Table 4.5 shows the comparison table. Note that direct comparison between the measured value and [36] is not accurate because 1) the relationship between the deposited energy and

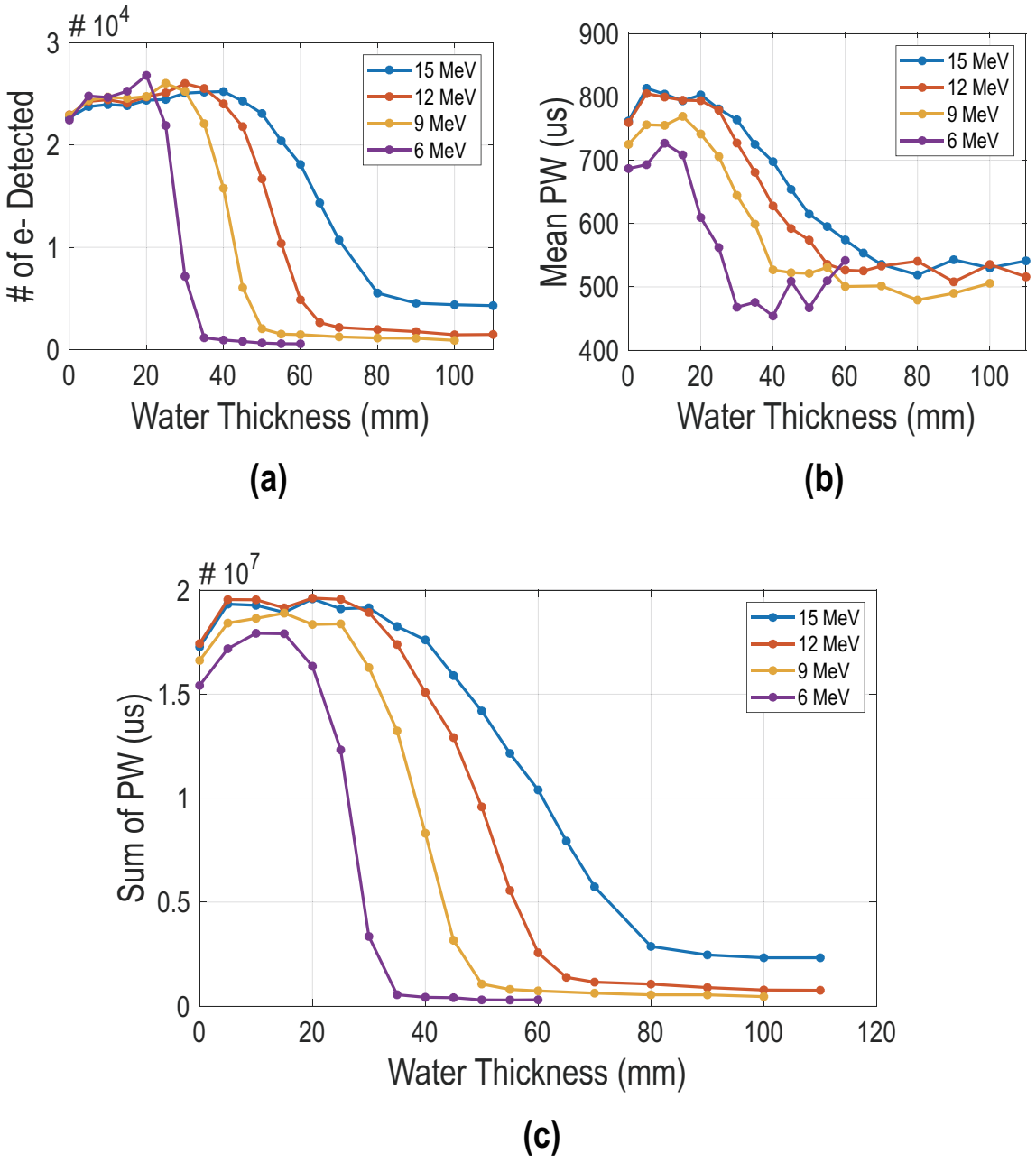

Figure 4.18: Measured mean PW, flux, and summation of PW at 6, 9, 12, and 15 MeV electron beam.

PW is logarithmic, 2) the distance between the source and sensor is much smaller in [36] than that in our experiment setup, and 3) this work uses 3 mm Cerrobend collimator that changes the shape of the depth-dose curve. However, the trends as the energy goes from 6

	This work				Fig. 6 in [36]			
Energy (MeV)	6	9	12	15	6	9	12	15
D_{surf} (%)	86	88	89	89	78.6	78.5	85.7	89.9
z_{max} (mm)	13	15	20	25	14	23	30	32
R_{90} (mm)	21	27.5	34	40	20	30	41	50
R_{50} (mm)	27	39	50	62	23	37	48	62
R_{max} (mm)	35	55	70	85	33	50	65	83
D_B (%)	2.25	3.3	5.39	11.8				

Table 4.5: Comparison between the measured result and [36].

to 15 are similar.

4.5 Beta-particle Measurement Results (Lutetium-177)

The ability to measure single beta-particles is critical not only during the EBRT, but plays significant roles in theranostics (therapeutic + diagnostic). Most of the current state-of-the-art theranostics use beta-particle emitters, such as Lu-177 or Y-90. The radionuclides combined with tumor-specific antibodies attach to tumor cells and the location of the tumor can be estimated by measuring the radiation. Radionuclides that emit both beta-particles and photons has been widely used because the photons can be monitored externally using a SPECT imager. However, the spatial and temporal resolution are limited. In addition, this limits the choice of radionuclides because they should include X-ray emissions in its decay chain.

All radionuclides go under radioactive decay. For any large enough number of radionuclides, the decay characteristic can be statistically determined. The activity, $A(t)$, can be expressed as

$$A(t) = -\frac{dN(t)}{dt} = \lambda N(t), \tag{4.1}$$

where $N(t)$ is the total number of radionuclides that have not decayed and λ is the decay constant. This leads to

$$\begin{aligned} N(t) &= N_0 e^{-\lambda t} \\ A(t) &= A_0 e^{-\lambda t}, \end{aligned} \tag{4.2}$$

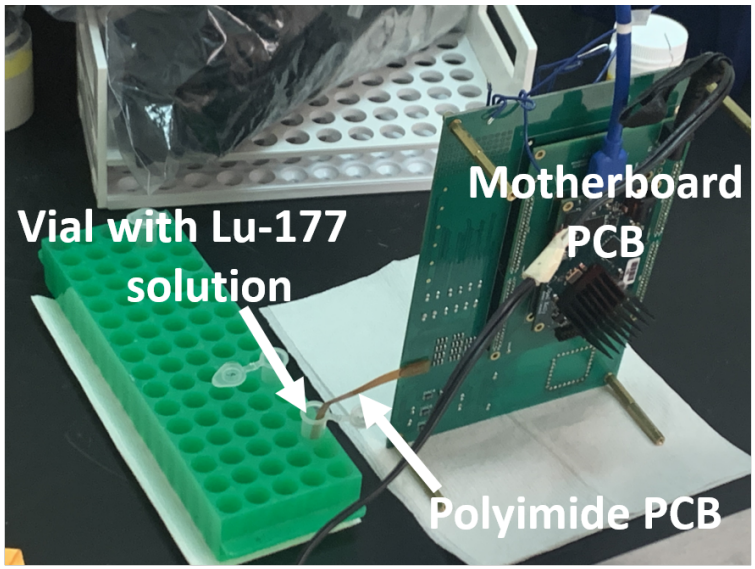

Figure 4.19: Lu-177 solution measurement setup.

where N_0 and A_0 are initial number of radionuclides and activity, respectively. The activity of the decay decreases exponentially, and half-life can be defined as

$$N(t) = N_0(\frac{1}{2})^{t/t_{half}}, \tag{4.3}$$

where t_{half} is the half-life. Combining Eq. 4.2 and 4.3, we obtain

$$t_{half} = \frac{\ln 2}{\lambda}. \tag{4.4}$$

Suppose that an ideal detector counts the number of radioactive emissions from $t = t_1$ to $t = t_2$. Then, the average activity during the measurement that the detector will see is

$$\begin{aligned} A_{mean} &= \frac{\int_{t_1}^{t_2} A(t)dt}{t_2 - t_1} \\ &= \frac{\int_{t_1}^{t_2} A_0 e^{-\lambda t}dt}{t_2 - t_1} \\ &= \frac{(e^{-t_1\lambda} - e^{-t_2\lambda})A_0}{\lambda(t_2 - t_1)}, \end{aligned} \tag{4.5}$$

where A_{mean} is the average activity.

Fig. 4.19 shows the Lu-177 solution measurement setup photo. The polyimide PCB is placed in the Lu-177 solution, and we make sure that the chip is completely submerged. After

a measurement is finished, the polyimide PCB is gently wiped with a tissue and submerged in the next vial.

Seven vials with different concentration of Lu-177 are initially measured. To minimize the device mismatch and contamination from the previous measurement, the same chip is used to measure 7 vials from the lowest concentration to the highest concentration. Table 4.6 shows the measurement results. Because the half-life of the Lu-177 is 6.647 days, additional measurements for 4 vials are done after a week (1^*, 2^*, 3^*, and 4^* in the table). The initial activities of the vials are measured using Capintec CRC-15R Dose Calibrator. Mean activity is the estimated activity when the chip measures using Lu-177 half-life and Eq. 4.5. Each vial is measured for at least 40 minutes to have enough data.

The percent injected dose (ID) per gram (%ID per gram) is a metric to evaluate the effectiveness of the tumor specific antibody. It represents what percentage of the injected dose stays in the tumor, normalized by the tumor weight. Depending on the type of antibody and mouse characteristics (i.e. blood flow, age, and density of receptors), the %ID per gram value typically varies from $\sim$2 to $\sim$50. Assuming the total injected dose of 800 μCi, the tumor density of 1 g/cm^3, and the tumor weight of 0.5 gram, 10 %ID/g corresponds to 40 μCi of activity in the tumor with 0.08 μCi/μL concentration. As shown in Table 4.6, the experiment covers a wide range of %ID/g value.

The violation rate stays low at around 0.4 %, meaning that most data are valid and from single electron hit. Mean PWs of each vial are consistent at around 1,600 μs. Total count and count per minute (CPM) values are also displayed. More importantly, The CPM should be proportional to the Lu-177 concentration, and CPM per concentration values range from 1,202 to 1,351 #μL/μCi/min except the vial 7, which has the lowest concentration. We hypothesize that the reasons why the vial 7 has higher CPM per concentration value than others are: 1) due to background radiation in the room, as CPM of vial 7 is extremely low (1 count per minute) and 2) inaccurately measured initial activity at such a low concentration. Note that because the initial concentration of the vial 7 is lower than the threshold of CRC-15R machine, the activity is estimated based on how we diluted the solution. However, the %ID/g value for vial 7 (0.047) is much lower than the typical value of state-of-the-art tumor specific antibodies.

Fig. 4.20 depicts the measured %ID/g versus CPM. The curve is linear across wide range from $\sim$0.2 to 140 %ID/g as expected. In each data set, standard deviations of CPM at every 5 minutes are calculated. $\pm 1\ \sigma$ range is plotted for each data point. As %ID/g increases, the variation of CPM decreases due to having more hits.

	Vials										
	1	2	3	4	5	6	7	1*	2*	3*	4*
Initial Activity (μCi)	818	311	78.7	20.7	5.6	1.4	0.47	818	311	20.7	5.6
Volume (μ L)	400	600	600	600	600	600	800	400	600	600	600
Concentration (μCi/μL)	2.045	0.518	0.131	0.0345	0.0093	0.0023	0.0006	2.045	0.518	0.131	0.0345
Mean Activity (μCi)	467.379	178.463	49.203	12.988	3.529	0.886	0.300	249.314	95.138	24.158	6.375
Mean Concentration (μCiμL)	1.168	0.297	0.0820	0.0216	0.0059	0.0015	0.0004	0.623	0.159	0.0403	0.0106
Percent ID per Gram (%ID/g)	146.056	37.180	10.251	2.706	0.735	0.185	0.047	77.911	19.820	5.033	1.328
Measurement Time (min)	48.217	65.167	47.750	47.467	67.333	52.667	101.683	51.950	46.633	44.600	41.467
Violation Rate (%)	0.368	0.346	0.343	0.515	1.468	0	0	0.344	0.363	0.261	0.801
Mean PW (μs)	1,601	1,654	1,587	1,606	1,559	1,441	1,424	1,579	1,630	1,653	1,605
Total Count (#)	72,877	26,189	5,224	1,354	476	102	98	41,320	9,795	2,345	476
CPM (#/min)	1,511	401.9	109.4	285	7.1	1.9	1.0	795.4	210.0	52.6	13.4
CPM per Concentration (#μL/μCi/min)	1,294	1,351	1,334	1,318	1,202	1,311	2,570	1,276	1,325	1,306	1,202

Table 4.6: Lu-177 solution measurement results.

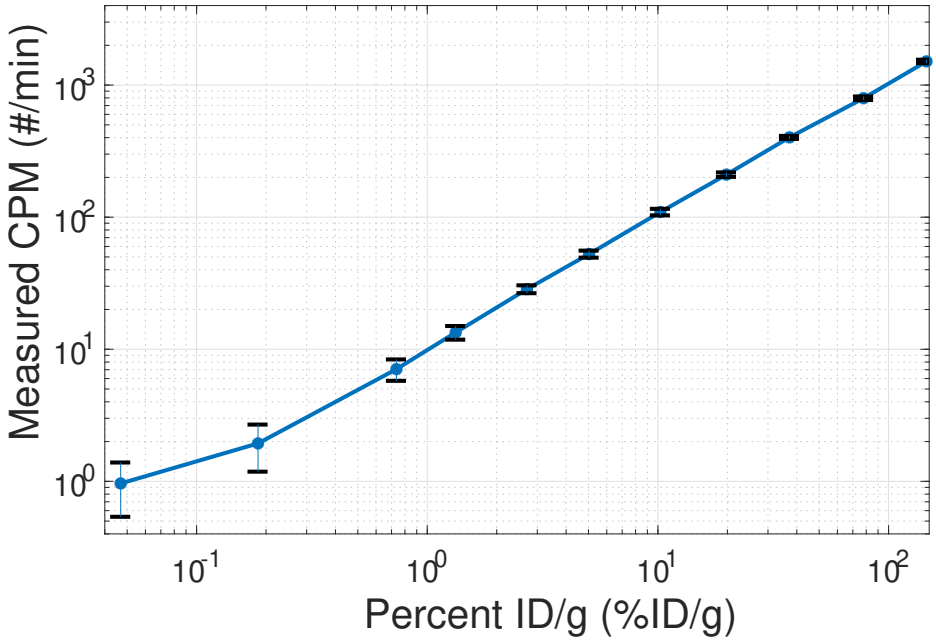

Figure 4.20: Measured Lu-177 concentration versus count per minute.

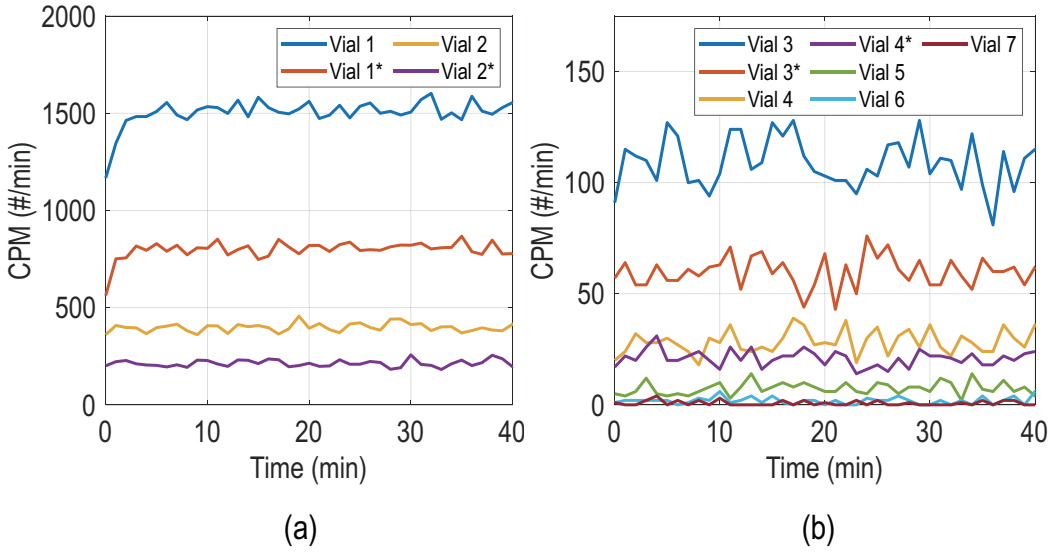

Figure 4.21: Measured Lu-177 time domain plots.

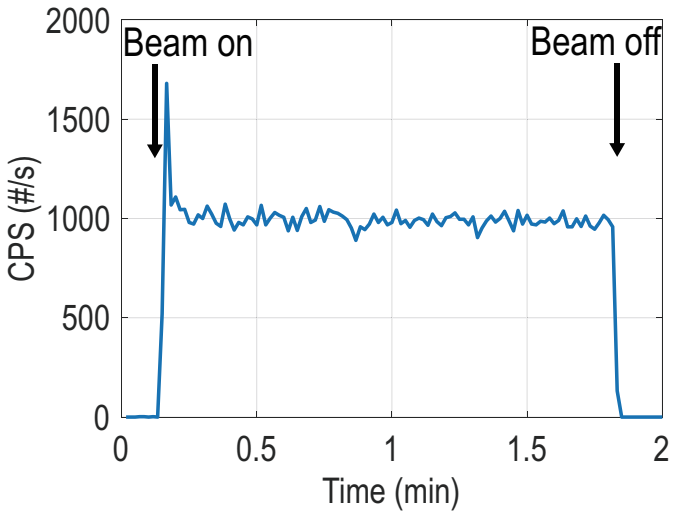

Figure 4.22: Measured X-ray time domain plot.

Fig. 4.21 shows the time domain CPM plots for 40 minutes of each data set with sampling period of 1 minute. For vials 1, 1*, and 2, it takes about 3 minutes for the Lu-177 solution to fully combine with the new solution, and reach the steady state. Note that the Lu-177 half life and the time it takes to reach steady state in the tumor are much longer than 3 minutes. After reaching the steady state, the CPM stays stable.

4.6 X-ray Measurement Results

Even though X-rays can be measured outside of the patient as X-rays penetrate through the whole body, *in vivo* X-ray monitoring is important. For example, the device can monitor whether X-ray photons are hitting the target as planned during EBRT.

An X-ray photon itself does not deposit not much energy into matter. Secondary electrons produced by photoelectric effect, Compton scattering, or pair production are the major mechanism of energy depositions by X-ray photons [21]. We hypothesize that the device is capable of measuring photons via secondary electrons.

To verify the functionality, the device was radiated by 6 MeV X-ray beam from Siemens linear accelerator. Note that because the linear accelerator produces X-ray using Bremsstrahlung radiation, where X-ray photon is produced when a high speed electron is deflected off of its trajectory by Columbic force from the nuclei, the X-ray beam is not mono-energetic.

Fig. 4.22 depicts measured time-domain count per second (CPS) plot of 6 MeV X-ray beam. The total dose is 5 Gy with the dose rate of 3 Gy/min. The CPS value rises rapidly right after the beam is on and saturates at around 1,000 #/s. It then quickly collapses to 0 when the beam is turned off.

Chapter 5

Conclusion

5.1 Summary

In this dissertation, we have described a millimeter-scale single-charged particle dosimeter that was fabricated in 65 nm CMOS technology. We discussed how the ability to measure with single particle sensitivity is critical for clinical cancer radiotherapy, including EBRT and TRT. In brief, EBRTs, such as proton beam therapy and hadron therapy, suffer from inaccurate prediction of the location of the Bragg peak which depends on many factors (i.e. patient movements or anatomical characteristics). One of the biggest challenge of using TRT is to know tumor uptake with enough spatiotemporal resolution and accumulated dose in organs at high risks. The proposed system solves these problems by measuring the true dose inside the body in real time, making the closed-loop treatment with much better efficiency and safety. We also described the theoretical background of how charged particles and photons interact with matter, and how they can be measured using a diode.

To demonstrate, we designed, fabricated, and verified the detector ASIC. We made an array of very small diodes in a chip to improve the sensitivity and have enough detection area at the same time. More importantly, instead of measuring the voltage drop caused by particle hit, pulse-width sensing strategy was used to avoid power-hungry and bulky analog-to-digital converters. This makes the system power consumption low. In addition, by using in-pixel SRAM, we can easily disable pixels that give false positive signals due to PVT variations.

Additionally, to prove the functionality of the proposed system, we tested the prototype using clinical proton, electron, and X-ray beams. As expected, the logarithmic relationship between the PW and energy deposition was shown for the proton beam. The system was also verified using Lu-177 radionuclide solution, and the measured electron count is proportional to the concentration over the wide clinical range.

The prototype ASIC uses only conventional chip fabrication technology that has been widely used in integrated circuit applications such as CPUs and smartphone chips. Therefore, it is expected to have low cost for high volume manufacturing with reliable operation.

Table 5.1: Comparison table with state-of-the-art.

	[7]	[8]	[9]	[10]	*This work*
Sensing method	Vth shift	Vth shift	RL/OSL	Floating gate	Diode
Sensing area (mm^2 or mm^3)	0.3×0.05	0.2×0.2	0.5×0.5×2	0.1×0.08	0.512×0.512
Power consumption for sensing (mW)	N/A (Passive)	N/A (Passive)	4 (low), 16 (peak)	2	0.535
Power supply (V)	N/A	N/A	N/A	1.2	1.2
Real time?	No	Yes	Yes	Yes	Yes
Single particle detection?	**No**	**No**	**No**	**No**	**Yes**

5.2 Comparison

The prototype ASIC consumes average static powers of 505 μW, 28 μW, and 2 μW for the analog pixel array, digital system, and FLL, respectively. A comparison table with state-of-the-art dosimeters are summarized in Table 5.1. This work has the second largest sensing area of $0.512\times0.512\,mm^2$, the lowest power consumption among active sensors, and the capability of detecting radiation in real time. Most importantly, this work is the first work that can detect energy deposition by single charged particles with a form-factor and the power consumption compatible with wireless *in vivo* dosimeter for cancer therapy.

5.3 Future Directions

Personalized dosimeter for cancer radiotherapy can play a critical role both in treatment and research. For example, the proposed system can be used to monitor the real time biodistribution over several half-lives for a newly developed radionuclide solution. In addition, the ability to monitor the single particle can be used in analyzing the true biological effect by single particles *in vivo*. However, a number of technical challenges remain before the commercialization of the device.

Using PIN diode

The prototype used a conventional general purpose CMOS fabrication technology. This can be advantageous because it ensures reliable operations for high-volume manufacturing in the future with relatively low cost. However, using a fabrication technology that provides a PIN diode can enhance the sensitivity of the device. For example, a diode with 10 times thicker depletion region gives 10 times more energy deposition and 10 times lower parasitic capacitance, leading to having 100 times more signal. As a result, it improves the overall SNR by 10 times.

The amount of energy that a charged particle deposits in a thin matter is a stochastic process and has a wide Landau distribution [28]. This means that there is a probability

that the particle deposits very small energy. Currently, the device measures with a threshold to minimize the false-positive signal generated from the noise. PIN-diode based design can be useful in detecting small LET, especially for electrons. However, because fabrications providing the PIN-diode design typically have relatively large minimum transistor channel length (i.e., XFAB's 350 nm photodiode process), reducing the fill factor and overall area will be challenging.

Measuring the Absolute Energy Deposition

This dissertation introduced a novel PW-sensing strategy that obviates the need for fast ADCs. This helps reduce the overall power consumption and design complexity. The final data are combinations of the particle energy distribution as well as added uncertainties, the Landau distribution, electrical noise, pixel-to-pixel variation, logarithmic relationship between the PW and the energy deposition, incident angle, and the shape of the depletion region. As a result, the data is the relative measurement of the actual energy deposition.

To be able to measure the true dose deposition, calibrations to minimize the aforementioned uncertainties are necessary. The pixel-to-pixel variation and logarithmic relationship can be effectively mitigated by measuring mono-energetic high LET charged particle at different particle energies and calibrating based on the measured data. However, measuring the thickness and shape of the depletion region is challenging because: 1) energy deposition has its own probability distribution, 2) the detection threshold should be accurately measured, and 3) it is difficult to know the single particle trajectory because the signal is angle-dependent.

To address this issue, comparing the measured data with Monte-Carlo simulation and data measured by an off-the-shelf silicon detector is needed. For example, in order to know the exact particle flux and energy at a certain location, a silicon detector with known specifications (i.e., noise, detection threshold, and depletion region thickness) can measure a radiation source. Using this data, accurate simulation model can be constructed and the simulation result can verify the data measured with our prototype.

Wireless Design

Eventually, the IVD needs to be wirelessly implemented for chronic long-term monitoring of the dose deposition in the body. Power and data harvesting through electromagnetic wave (EM wave) or ultrasound can be considered. The Food and Drug Administration (FDA) energy density safety limits are 10 mW/mm^2 and 720 mW/mm^2 for the EM wave and ultrasound, respectively. In addition, smaller wavelength and better path loss in tissue make the ultrasonic approach preferable. With the same transmitted power, the ultrasound penetrates much deeper in the tissue. Therefore, a piezoelectric material with an AC to DC converter powers the device. Data communication can be done using a backscatter method.

Closing Remark

Despite the remaining issues that need to be addressed, this dissertation demonstrated the principle of a single charged-particle radiation detector using a 64×64 diode array. The proposed concept can be effectively used in making a real time closed loop control of existing cancer radiotherapies. Uncertainties in delivering the right amount of dose while minimizing damages to healthy cells is currently the biggest challenge. The proposed device makes the treatment personalized that can effectively minimize those uncertainties. We hope that the proposed system paved a way for future potential realization of cancer radiotherapies.

Bibliography

[1] K. Lee, J. Scholey, E. B. Norman, I. K. Daftari, K. K. Mishra, B. A. Faddegon, M. M. Maharbiz, and M. Anwar, "A 64×64 Implantable Real-Time Single-Charged-Particle Radiation Detector for Cancer Therapy," *IEEE International Solid-State Circuits Conference (ISSCC)*, 2020.

[2] K. Lee, J. Scholey, E. B. Norman, I. K. Daftari, K. K. Mishra, B. A. Faddegon, M. M. Maharbiz, and M. Anwar, "A Millimeter-scale Single Charged Particle Dosimeter for Cancer Radiotherapy," *IEEE Journal of Solid-State Circuits (JSSC)*, 2020.

[3] "Cancer Facts & Figures 2021," Report from *American Cancer Society*, 2021.

[4] "Cancer Treatment & Survivorship Facts & Figures 2019-2021," Report from *American Cancer Society*, 2021.

[5] W. Newhauser and R. Zhang, "The Physics of Proton Therapy," *Physics in Medicine and Biology*, vol. 60, pp. R155-R209, 2015.

[6] M. Yang, X. R. Zhu, P. C. Park, U. Titt, R. Mohan, G. Virshup, J. E. Clayton, and L. Dong, "Comprehensive analysis of proton range uncertainties related to patient stopping-power-ratio estimation using the stoichiometric calibration," *Physics in Medicine and Biology*, vol. 57, pp. 4095-4115, 2012.

[7] G. Beyer, G. G. Mann, J. A. Pursley, and E. T. Espenhahn, "An Implantable MOSFET Dosimeter for the Measurement of Radiation Dose in Tissue During Cancer Therapy," *IEEE Sensors Journal*, vol. 8, pp. 38-51, 2008.

[8] E. Gurp, B. K. C. Haanstra, L. H. P. Murrer, F. C. J. M. . van Gils, A. L. A. J. Dekker, B. J. Mijnheer, and P. Lambin, "In Vivo Dosimetry with a Linear MOSFET Array to Evaluate the Urethra Dose During Permanent Implant Brachytherapy Using Iodine-125," *International Journal of Radiation Oncology Biology Physics*, vol. 75, no. 4, pp.1266-1272, 2009.

[9] C. Andersen, S. K. Nielsen, S. Greilich, J. Helt-Hansen, J. C. Lindegaard, and K. Tanderup, "Characterization of a Fiber-coupled Al_2O_3:C Luminescence Dosimetry System for Online In Vivo Dose Verification during ^{192}Ir Brachytherapy," *Medical Physics*, vol. 36, pp. 708-718, 2009.

[10] A. Shamim, M. Arsalan, L. Roy, M. Shams, and G. Tarr, "Wireless Dosimeter: System-on-Chip Versus System-in-Package for Biomedical and Space Applications," *IEEE Transactions on Circuits and Systems II*, vol. 55, pp. 643-647, 2008.

[11] E. Grusell and J. Medin, "General Characteristics of the Use of Silicon Diode Detectors for Clinical Dosimetry in Proton Beams," *Physics in Medicine and Biology*, vol. 45, pp. 2573-2582, 2000.

[12] L. Wang, L. A. Perles, L. Archambault, N. Sahoo, D. Mirkovic, and S. Beddar, "Determination of the Quenching Correction Factors for Plastic Scintillation Detectors in Therapeutic High-energy Proton Beams," *Physics in Medicine and Biology*, vol. 57, pp.7767-7781, 2012.

[13] D.T. Goodhead, R. J. Munson, J. Thacker, and R. Cox, "Mutation and Inactivation of Cultured Mammalian Cells Exposed to Beams of Accelerated Heavy Ions IV. Biophysical Interpretation," *International Journal of Radiation Biology*, vol. 37(2), pp. 135-167, 1980.

[14] D.T. Goodhead, "Initial Events in the Cellular Effects of Ionizing Radiations: Clustered Damage in DNA," *International Journal of Radiation Biology*, vol. 65, pp. 7-17, 1994.

[15] NIST pstar, https://physics.nist.gov/PhysRefData/Star/Text/PSTAR.html. Accessed 14 July 2021.

[16] NIST estar, https://physics.nist.gov/PhysRefData/Star/Text/ESTAR.html. Accessed 14 July 2021.

[17] E.J. Hall, "Radiobiology for the Radiologist, 7th Edition" *Hagerstown, Md. :Medical Dept., Haper & Row*, 2012.

[18] Annunziata, M. F, "Radioactivity: Introduction and History" *Boston, Elsevier*, 2007.

[19] Turner, E. J., "Atoms, Radiation, and Radiation Protection" *Wiley*, 2007.

[20] Simon R. C. , James A. S. , and Michael E. P. , "Physics in Nuclear Medicine" *Elsevier*, 2012.

[21] E. J. Hall and A. J. Giaccia, "Radiobiology for Radiologists" *Wolters Kluwer*, 2018.

[22] R. C. Alig and S. Bloom, "Electron-hole-pair creation energies in semiconductors," *Physics Review Letters*, vol. 35, pp.1522-1525, 1975.

[23] M. Zhang C. Chan, Y. Zhu, and R. P. Martins, "A 0.6V 13b 20MS/s Two-Step TDC-Assisted SAR ADC with PVT Tracking and Speed-Enhanced Techniques," *International Solid-State Circuits Conference (ISSCC), 2019.*

[24] I.K. Daftari, K. K. Mishra, R. P. Singh, D. J. Shadoan, and T. L. Phillips, "An Overview of the Control System for Dose Delivery at the UCSF Dedicated Ocular Proton Beam," *International Journal of Medical Physics*, vol. 5, pp. 242-262, 2016.

[25] I.K. Daftari, C. M. Castaneda, T. Essert, T. L. Phillips, and K. K. Mishra, "Scintillator-CCD Camera System Light Output Response to Dosimetry Parameters for Proton Beam Range Measurement," *Nuclear Instruments and Methods in Physics Research A*, vol. 686, pp. 7-14, 2012.

[26] B.A. Faddegon, J. Shin, C. M. Castenada, J. Ramos-Mendez, and I. K. Daftari, "Experimental Depth Dose Curves of a 67.5 MeV Proton Beam for Benchmarking and Validation of Monte Carlo Simulation," *Medical Physics*, vol. 42, pp. 4199-4210, 2015.

[27] W. Biederman, D. J. Yeager, N. Narevsky, A. C. Koralek, J. M. Carmena, E. Alon, and J. M. Rabaey, "A Fully-Integrated, Miniaturized ($0.125\,\mathrm{mm}^2$) 10.5 uW Wireless Neural Sensor," *IEEE Journal of Solid-State Circuits*, vol. 48, pp. 960-970, 2013.

[28] L. Landau, "On the Energy Loss of Fast Particles by Ionization," *Journal of Physics*, vol. 8, 1944.

[29] TOPAS : tool for particle simulation : http://topasmc.org

[30] J. Perl, J. Shin, J. Schumann, B. A. Faddegon, and H. Paganetti, "TOPAS - An Innovative Proton Monte Carlo Platform for Research and Clinical Applications," *Medical Physics*, vol. 39, pp. 6818-6837,2012.

[31] B. Faddegon, J. Ramos-Mendez, J. Schuemann, A. Mcnamara, J. Shin, J. Perl, and H. Paganetti, "The TOPAS Tool for Particle Simulation, a Monte Carlo Simulation Tool for Physics, Biology and Clinical Research," *Physica Medica: European Journal of Medical Physics*, vol. 72, pp. 114-121, 2019.

[32] S. Agostinelli et al., "GEANT4 - A Simulation Toolkit," *Nuclear Instruments and Methods in Physics Research Section A*, vol. 506, pp. 250-303, 2003.

[33] J. Allison et al., "GEANT4 Developments and Applications," *IEEE Transactions on Nuclear Science*, vol. 53, pp. 270-278, 2006.

[34] J. Allison et al., "Recent Developments in GEANT4," *Nuclear Instruments and Methods in Physics Research Section A*, vol. 835, pp. 186-225, 2016.

[35] S. Garcia, "Dosimetry Dust: An Ultrasonic Backscatter Implantable Dosimetry Device," *EECS Department, University of California, Berkeley*, 2017.

[36] B. A. Faddegon, D. Sawkey, and T. O'shea, "Treatment Head Disassembly to Improve the Accuracy of Large Electron Field Simulation," *Medical Physics*, vol. 36, pp. 4577-4591, 2009.

[37] E. B. Podgorsak, "Radiation Oncology Physics: A Handbook for Teachers and Students," *IAEA*.

[38] E. A. M. Ruigrok, W. M. van Weerden, J. Nonnekens, and M. de Jong , "The Future of PSMA-Targeted Radionuclide Therapy: An Overview of Recent Preclinical Research," *Pharmaceutics*, vol. 11, 2019.

[39] S. R. Banerjee, V. Kumar, A. Lisok, J. Chen, I. Minn, M. Brummet, S. Boinapally, M. Cole, E. Ngen, B. Wharram, C. Brayton, R. F. Hobbs, and M. G. Pomper, "177Lu-labeled low-molecular-weight agents for PSMA-targeted radiopharmaceutical therapy," *European Journal of Nuclear Medicine and Molecular Imaging*, vol. 46, pp. 2545-2557, 2019.